

Density matrix renormalization group study in energy space for a single-impurity Anderson model and an impurity quantum phase transition

Tomonori Shirakawa¹ and Seiji Yunoki^{1,2,3}

¹*Computational Quantum Matter Research Team,*

RIKEN Center for Emergent Matter Science (CEMS), Wako, Saitama 351-0198, Japan

²*Computational Condensed Matter Physics Laboratory, RIKEN, Wako, Saitama 351-0198, Japan*

³*Computational Materials Science Research Team,*

RIKEN Advanced Institute for Computational Science (AICS), Kobe, Hyogo 650-0047, Japan

(Dated: June 23, 2016)

The density matrix renormalization group method is introduced in energy space to study Anderson impurity models. The method allows for calculations in the thermodynamic limit and is advantageous for studying not only the dynamical properties but also the quantum entanglement of the ground-state at the vicinity of an impurity quantum phase transition. This method is applied to obtain numerically exactly the ground-state phase diagram of the single-impurity Anderson model on the honeycomb lattice at half-filling. The calculation of local static quantities shows that the phase diagram contains two distinct phases, the local moment (LM) phase and the asymmetric strong coupling (ASC) phase, but no Kondo screening phase. These results are supported by the local spin and charge excitation spectra, which exhibit qualitatively different behavior in these two phases and also reveal the existence of the valence fluctuating point at the phase boundary. For comparison, we also study the low-energy effective pseudogap Anderson model using the method introduced here. Although the high-energy excitations are obviously different, we find that the ground-state phase diagram and the asymptotically low-energy excitations are in good quantitative agreement with those for the single-impurity Anderson model on the honeycomb lattice, thus providing a quantitative justification for the previous studies based on low-energy approximate approaches. Furthermore, we find that the lowest entanglement level is doubly degenerate for the LM phase, whereas it is singlet for the ASC phase and is accidentally three fold degenerate at the valence fluctuating point. This should be contrasted with the degeneracy of the energy spectrum because the ground-state is found to be always singlet. Our results therefore clearly demonstrate that the low-lying entanglement spectrum can be used to determine with high accuracy the phase boundary of the impurity quantum phase transition.

PACS numbers: 75.20.Hr, 73.22.Pr, 75.30.Hx

I. INTRODUCTION

Recent experiments have revealed that the introduction of adatoms induces the local magnetic moments in graphene [1, 2]. One of the simplest models describing the magnetic impurity problem in graphene is an Anderson impurity coupled to the conduction electrons on the honeycomb lattice with the massless Dirac energy dispersion which results in the linear density of states ($\propto |\omega|$) around the Fermi level [3]. This problem is known as the pseudogap Kondo problem [4] and has been studied extensively for over a decade by the renormalization group analysis [5, 6] and the numerical renormalization group (NRG) method [7–11]. These previous studies have already found that, at zero temperature, there exit two phases, i.e., the local moment (LM) phase and the asymmetric strong coupling (ASC) phase, and the phase boundary corresponds to the valence fluctuating (VF) point [7].

These studies are, however, based on the low-energy effective pseudogap Anderson models [4] and focused mostly on the two special cases in the large conduction band limit and in the strong coupling limit [7–10]. Although the essential part of Kondo physics should be captured in these low-energy analyses, it is rather surprising

that the phase diagram even for the simplest and most fundamental Anderson impurity model, not for the low-energy effective models, has not been established so far. The reason is simply because of lack of reliable numerical methods which can treat Anderson impurity models numerically exactly in two and three spatial dimensions. Establishing the numerically exact ground state phase diagram of the Anderson impurity model is also beneficial to the previous studies based on the low-energy effective models since it can provide a strong justification for their approximations.

On the other hand, the entanglement spectrum [12] has attracted much attention recently in condensed matter physics for identifying topologically ordered phases [12–16]. In these systems, the degeneracy of the low-lying entanglement spectrum is intimately related to the existence of the surface boundary states which are protected by bulk symmetries. Since the magnetic impurity problem can be regarded as a boundary problem in one dimension [17], it is also valuable to explore its quantum entanglement aspects. In this context, the recent study of a “spin-only” version of a two-impurity Kondo model has shown that the gap of the entanglement spectrum can be regarded as an order parameter [18]. The entanglement spectrum is thus expected to be also used to

quantify different quantum phases in magnetic impurity models including Anderson impurity models [19].

The main purposes of this paper are threefold. First, we introduce a numerical method which enables us to treat exactly general Anderson impurity models in any spatial dimension in the thermodynamic limit. Secondly, we demonstrate the method developed here by applying it to one of the simplest Anderson impurity models in two spatial dimensions and compare the results with those for the low-energy effective pseudogap Anderson model. Third, we explore the impurity quantum phase transition and the low-lying entanglement spectrum to uncover the degeneracy of the lowest entanglement level across the impurity quantum phase transition.

To this end, here we introduce the density matrix renormalization group (DMRG) method [20, 21] for general Anderson impurity models represented in energy space. This method is applied to the single-impurity Anderson model on the honeycomb lattice at half-filling to determine precisely the ground-state phase diagram in a wide range of parameters, including an intermediate coupling region. The calculations of the local static quantities reveal that the phase diagram contains only two phases, i.e., the LM and ASC phases. The local spin and charge excitation spectra further support these results and also show the existence of the VF point at the phase boundary. We also study the low-energy effective pseudogap Anderson model and compare the ground-state phase diagram as well as the local spin and charge excitation spectra with those for the single-impurity Anderson model on the honeycomb lattice. Although the high-energy excitations are apparently different, the ground-state phase diagrams and the asymptotically low-energy excitations for these two models are found to be in excellent quantitative agreement. Moreover, we find that the degeneracy of the lowest entanglement level is different in the three different regions of the phase diagram, i.e., the LM and ASC phases and the VF point. This is in sharp contrast to the degeneracy of the ground state, which is found always singlet in all three regions. Although it has been pointed out that the sudden change of entanglement properties is not always related to quantum phase transition [22], our results demonstrate that the low-lying entanglement spectrum can be used to determine the impurity quantum phase transition, at least, between the LM and ASC phases.

The rest of this paper is organized as follows. First, the single-impurity Anderson model on the honeycomb lattice and the corresponding low-energy effective pseudogap Anderson model are introduced in Sec. II. The DMRG method to solve general Anderson impurity models in energy space is also described in details in Sec. II. The numerical results for the single-impurity Anderson model on the honeycomb lattice are shown in Sec. III. Based on the local static properties shown in Sec. III B, the ground-state phase diagram is established in Sec. III C. The local spin and charge excitation spectra are also calculated in Sec. III D to support the

phase diagram. Furthermore, these results are compared with those for the low-energy effective pseudogap Anderson model in Sec. III E. Finally, the low-lying entanglement spectrum and the entanglement entropy for the single-impurity Anderson model on the honeycomb lattice are discussed in Sec. III F before summarizing the paper in Sec. IV. The energy space description of the single-impurity Anderson model is discussed in Appendix A and the further technical details of numerical calculations are provided in Appendix B.

II. MODELS AND METHOD

In this section, we first introduce the single-impurity Anderson model on the honeycomb lattice. Considering this model as an example, we describe in details the DMRG method in energy space, which can treat exactly general Anderson impurity models in any spatial dimensions. We also introduce the pseudogap Anderson model as a low-energy effective model for the single-impurity Anderson model on the honeycomb lattice.

A. Single-impurity Anderson model

In order to be specific and also because it is one of the simplest models for the magnetic impurity problem in graphene, here we consider the single-impurity Anderson model on the honeycomb lattice [see Fig. 1(a)] defined by the following Hamiltonian:

$$\mathcal{H}_{\text{AIM}} = \mathcal{H}_i + \mathcal{H}_c + \mathcal{H}_V, \quad (1)$$

where the impurity Hamiltonian \mathcal{H}_i , including the on-site Coulomb interaction U and the on-site potential ε at the impurity site, is given as

$$\mathcal{H}_i = U n_{i,\uparrow} n_{i,\downarrow} - \varepsilon n_i, \quad (2)$$

the conduction band with the nearest-neighbor hopping t is described on the honeycomb lattice as

$$\mathcal{H}_c = -t \sum_{\langle \mathbf{r}, \mathbf{r}' \rangle} \sum_{\sigma=\uparrow, \downarrow} (c_{\mathbf{r}, \sigma}^\dagger c_{\mathbf{r}', \sigma} + \text{H.c.}), \quad (3)$$

and the hybridization between the impurity site and the conduction band is represented as

$$\mathcal{H}_V = V \sum_{\sigma=\uparrow, \downarrow} (c_{i, \sigma}^\dagger c_{\mathbf{r}_0, \sigma} + \text{H.c.}). \quad (4)$$

Here, $c_{\mathbf{r}, \sigma}^\dagger$ ($c_{\mathbf{r}, \sigma}$) is the creation (annihilation) operator of a conduction electron with spin σ ($=\uparrow, \downarrow$) at site \mathbf{r} on the honeycomb lattice and $c_{i, \sigma}^\dagger$ ($c_{i, \sigma}$) is the creation (annihilation) operator of an electron at the impurity site i with $n_{i, \sigma} = c_{i, \sigma}^\dagger c_{i, \sigma}$ and $n_i = n_{i, \uparrow} + n_{i, \downarrow}$. The sum in \mathcal{H}_c denoted by $\langle \mathbf{r}, \mathbf{r}' \rangle$ runs over nearest-neighbor pairs of conduction sites \mathbf{r} and \mathbf{r}' on the honeycomb lattice. Notice here that the impurity site is connected to only one

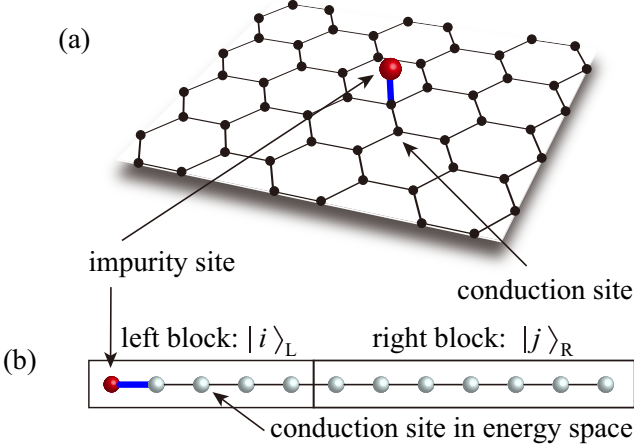


FIG. 1. (Color online) (a) Single-impurity Anderson model on the honeycomb lattice described by \mathcal{H}_{AIM} in Eq. (1). A red sphere and black dots represent the impurity site and the conduction sites, respectively. A blue line denotes the hybridization bond connecting the impurity site i and the conduction site \mathbf{r}_0 with the hybridization V in Eq. (4), and black lines represent the lattice bonds connecting the nearest-neighbor conduction sites on the honeycomb lattice with the hopping t in Eq. (3). (b) Single-impurity Anderson model in energy space described by \mathcal{H} in Eq. (20). Note that although the impurity site (a red sphere at the left edge) is described by the same impurity Hamiltonian \mathcal{H}_i in \mathcal{H}_{AIM} and is connected to only one of the conduction sites (gray spheres), the hybridization between the impurity site and the conduction site as well as the hopping between the conduction sites is generally different from those in (a). In the DMRG calculations, the system is divided into two parts, i.e., the left and right blocks, and the corresponding bases are denoted as $|i\rangle_L$ and $|j\rangle_R$.

of the conduction sites at \mathbf{r}_0 through the hybridization V in \mathcal{H}_V , as shown in Fig. 1(a). The electron density n is set to be half-filled, i.e., $n = 1$.

B. DMRG method in energy space

We first describe the Hamiltonian \mathcal{H}_{AIM} in energy space. This can be done by noticing that the effective action of the impurity site for \mathcal{H}_{AIM} can be reproduced exactly by, e.g., the following Hamiltonian:

$$\mathcal{H}_\omega = \mathcal{H}_i + \sum_{\sigma=\uparrow,\downarrow} \int d\omega \omega a_{\omega,\sigma}^\dagger a_{\omega,\sigma} + V \sum_{\sigma=\uparrow,\downarrow} \int d\omega \sqrt{\rho(\omega)} \left(c_{i,\sigma}^\dagger a_{\omega,\sigma} + \text{H.c.} \right), \quad (5)$$

where $a_{\omega,\sigma}^\dagger$ ($a_{\omega,\sigma}$) is the creation (annihilation) operator of a conduction electron which represents the eigenstate of \mathcal{H}_c with energy ω and spin σ , and the local density

of state per spin for the conduction band is denoted as $\rho(\omega)$ [7, 8]. The equivalence between \mathcal{H}_{AIM} and \mathcal{H}_ω is shown in Appendix A.

Next, we discretize the energy ω with the logarithmic discretization scheme

$$\omega_m^\pm = \pm \frac{W}{2} \Lambda^{-m}, \quad (6)$$

where W is the conduction band width ($W = 6t$ for the conduction band described by \mathcal{H}_c), $\Lambda (> 1)$ is a parameter which sets a series of intervals in ω_m^\pm 's with $m = 0, 1, \dots, M-1$ [23], and we set $\omega_M^\pm = 0$. Defining a representative fermion operator $a_{m,\pm,\sigma}^\dagger$ ($m = 1, 2, \dots, M$) for each energy interval between ω_{m-1}^\pm and ω_m^\pm , the Hamiltonian \mathcal{H}_ω can now be expressed as

$$\mathcal{H}_r = \mathcal{H}_i + \sum_{m=1}^M \sum_{\sigma=\uparrow,\downarrow} \left(\xi_m^+ a_{m,+,\sigma}^\dagger a_{m,+,\sigma} + \xi_m^- a_{m,-,\sigma}^\dagger a_{m,-,\sigma} \right) + \sum_{m=1}^M \sum_{\sigma=\uparrow,\downarrow} \left(\gamma_m^+ c_{i,\sigma}^\dagger a_{m,+,\sigma} + \gamma_m^- c_{i,\sigma}^\dagger a_{m,-,\sigma} + \text{H.c.} \right), \quad (7)$$

where

$$\gamma_m^\pm = V \left[\mp \int_{\pm\omega_m}^{\pm\omega_{m-1}} d\omega \rho(\omega) \right]^{1/2} \quad (8)$$

and

$$\xi_m^\pm = \frac{\int_{\pm\omega_m}^{\pm\omega_{m-1}} d\omega \rho(\omega) \omega}{\int_{\pm\omega_m}^{\pm\omega_{m-1}} d\omega \rho(\omega)}. \quad (9)$$

This discretization scheme is similar to the one employed in the NRG method [24]. The local density of states $\rho(\omega)$ for the conduction band can be calculated with desired accuracy by employing the linear tetrahedron method, as shown in Fig. 2 [25, 26].

Since we can use any discretization scheme to discretize the energy ω , we also introduce the constant discretization scheme

$$\omega_m^\pm = \pm \frac{W}{2} \left(1 - \frac{m}{M} \right) \quad (10)$$

with $m = 0, 1, \dots, M$. The logarithmic discretization scheme has much denser energy meshes as $|\omega|$ approaches to zero, but has much less energy meshes for larger $|\omega|$ away from zero. Therefore, in order to treat correctly the band structure in high-energy scales, the logarithmic discretization scheme requires small Λ close to 1, which is computationally demanding. In contrast, the constant discretization scheme distributes the energy meshes equally for all energy scales. We find that the logarithmic discretization scheme is suitable for the calculation of static quantities but the constant discretization scheme is better computationally to calculate dynamical quantities specially when the high-energy excitations are involved (see Appendix B for more details). It is also shown in Appendix A that the effective action of the impurity site

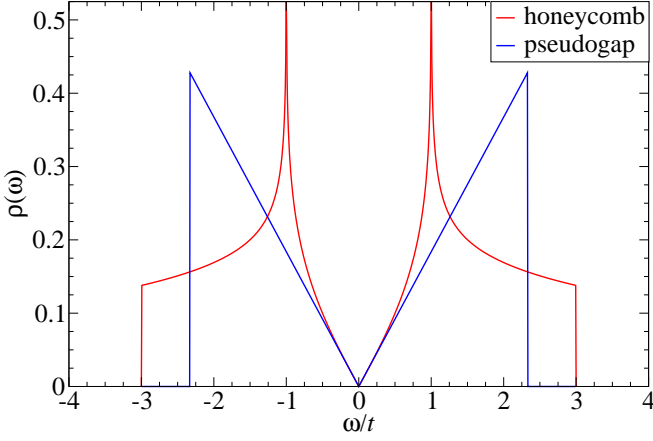


FIG. 2. (Color online) Local density of states $\rho(\omega)$ per spin for the conduction band of the single impurity Anderson model on the honeycomb lattice (red) and the pseudogap Anderson model (blue). Here, $W^2 = 4\sqrt{3}\pi t^2$ for the band width W of the pseudogap Anderson model. The Fermi energy is located at $\omega = 0$ for half filling.

for \mathcal{H}_r in both discretization schemes is exactly the same as the one for \mathcal{H}_{AIM} .

Finally, we transform the Hamiltonian \mathcal{H}_r into a one-dimensional form with no long-range hopping terms but keeping the interaction term local. For this purpose, we apply the Lanczos iteration [27] to the second and third terms in the right-hand side of \mathcal{H}_r with choosing the impurity site as the initial Lanczos basis vector. Introducing the vector representation of the electron creation and annihilation operators, e.g.,

$$\mathbf{a}_\sigma^\dagger = (c_{i,\sigma}^\dagger, a_{1,+,\sigma}^\dagger, a_{2,+,\sigma}^\dagger, a_{3,+,\sigma}^\dagger, \dots, a_{M-1,+,\sigma}^\dagger, a_{M,+,\sigma}^\dagger, a_{M,-,\sigma}^\dagger, a_{M-1,-,\sigma}^\dagger, \dots, a_{3,-,\sigma}^\dagger, a_{2,-,\sigma}^\dagger, a_{1,-,\sigma}^\dagger), \quad (11)$$

\mathcal{H}_r can be represented as

$$\mathcal{H}_r = \mathcal{H}_i + \sum_{\sigma=\uparrow,\downarrow} \mathbf{a}_\sigma^\dagger \hat{H}_0 \mathbf{a}_\sigma, \quad (12)$$

where \hat{H}_0 is a $(2M+1) \times (2M+1)$ matrix defined as

$$\hat{H}_0 = \begin{pmatrix} 0 & \gamma_1^+ & \gamma_2^+ & \gamma_3^+ & \cdots & \gamma_M^+ & \gamma_M^- & \cdots & \gamma_2^- & \gamma_1^- \\ \gamma_1^+ & \xi_1^+ & 0 & 0 & \cdots & 0 & 0 & \cdots & 0 & 0 \\ \gamma_2^+ & 0 & \xi_2^+ & 0 & \cdots & 0 & 0 & \cdots & 0 & 0 \\ \gamma_3^+ & 0 & 0 & \xi_3^+ & \cdots & 0 & 0 & \cdots & 0 & 0 \\ \vdots & \vdots & \vdots & \vdots & \ddots & \vdots & \vdots & \ddots & \vdots & \vdots \\ \gamma_M^+ & 0 & 0 & 0 & \cdots & \xi_M^+ & 0 & \cdots & 0 & 0 \\ \gamma_M^- & 0 & 0 & 0 & \cdots & 0 & \xi_M^- & \cdots & 0 & 0 \\ \vdots & \vdots & \vdots & \vdots & \ddots & \vdots & \vdots & \ddots & \vdots & \vdots \\ \gamma_2^- & 0 & 0 & 0 & \cdots & 0 & 0 & \cdots & \xi_2^- & 0 \\ \gamma_1^- & 0 & 0 & 0 & \cdots & 0 & 0 & \cdots & 0 & \xi_1^- \end{pmatrix} \quad (13)$$

Notice here that although the interaction term at the impurity site is described by the same impurity Hamiltonian \mathcal{H}_i , \mathcal{H}_r introduces long-range hopping terms as

the impurity site is hybridized with all conduction sites in energy space. This is usually problematic for DMRG calculations. As shown below, this can be completely alleviated by the Lanczos basis transformation without introducing additional long-range interaction terms for \mathcal{H}_i .

Taking as the initial Lanczos basis the $(2M+1)$ -dimensional column unit vector \mathbf{p}_1 with the k th element

$$(\mathbf{p}_1)_k = \delta_{k,1} \quad (k = 1, 2, \dots, 2M+1), \quad (14)$$

we can generate the Lanczos basis via the three-time recurrences

$$t_l \mathbf{p}_{l+1} = \hat{H}_0 \mathbf{p}_l - \varepsilon_l \mathbf{p}_l - t_{l-1} \mathbf{p}_{l-1} \quad (15)$$

for $l = 1, 2, \dots, L-1$ with $t_0 = 0$ and $\mathbf{p}_0 = 0$, where

$$\varepsilon_l = \mathbf{p}_l^T \hat{H}_0 \mathbf{p}_l \quad (16)$$

and

$$t_l = \left| \hat{H}_0 \mathbf{p}_l - \varepsilon_l \mathbf{p}_l - t_{l-1} \mathbf{p}_{l-1} \right|, \quad (17)$$

i.e., the norm of the $(2M+1)$ -dimensional column vector in the right-hand side of Eq. (15).

Using these Lanczos bases $\hat{P} = (\mathbf{p}_1, \mathbf{p}_2, \dots, \mathbf{p}_L)$, \hat{H}_0 can be transformed into the following tridiagonal matrix:

$$\hat{H}'_0 = \begin{pmatrix} \varepsilon_1 & t_1 & 0 & 0 & \cdots & 0 & 0 \\ t_1 & \varepsilon_2 & t_2 & 0 & \cdots & 0 & 0 \\ 0 & t_2 & \varepsilon_3 & t_3 & \cdots & 0 & 0 \\ 0 & 0 & t_3 & \varepsilon_4 & \cdots & 0 & 0 \\ \vdots & \vdots & \vdots & \vdots & \ddots & \vdots & \vdots \\ 0 & 0 & 0 & 0 & \cdots & \varepsilon_{L-1} & t_{L-1} \\ 0 & 0 & 0 & 0 & \cdots & t_{L-1} & \varepsilon_L \end{pmatrix} \quad (18)$$

and accordingly the electron creations operators $\mathbf{a}_\sigma^\dagger$ are transformed into the new operators $\mathbf{f}_\sigma^\dagger$ as

$$\mathbf{f}_\sigma^\dagger = (f_{1,\sigma}^\dagger, f_{2,\sigma}^\dagger, \dots, f_{L,\sigma}^\dagger) = \mathbf{a}_\sigma^\dagger \hat{P} \quad (19)$$

with $f_{1,\sigma}^\dagger = c_{i,\sigma}^\dagger$. Since $(\mathbf{p}_l)_k = (\hat{P})_{k,l}$ and $\mathbf{p}_l \cdot \mathbf{p}_{l'} = \delta_{l,l'}$, one can easily show that $(\hat{P}^T \hat{P})_{l,l'} = \delta_{l,l'}$. Therefore, the new operators $\mathbf{f}_\sigma^\dagger$ and \mathbf{f}_σ satisfy the fermion anticommutation relations, e.g., $\{f_{l,\sigma}, f_{l',\sigma'}^\dagger\} = \delta_{l,l'} \delta_{\sigma,\sigma'}$. Note also that $\varepsilon_1 = 0$ as $(\hat{H}_0)_{1,1} = 0$.

The resulting Hamiltonian after this basis transformation is

$$\mathcal{H} = \mathcal{H}_i + \sum_{\sigma=\uparrow,\downarrow} \sum_{l=1}^L \varepsilon_l f_{l,\sigma}^\dagger f_{l,\sigma} + \sum_{\sigma=\uparrow,\downarrow} \sum_{l=1}^{L-1} t_l (f_{l+1,\sigma}^\dagger f_{l,\sigma} + \text{H.c.}) \quad (20)$$

Notice first that the impurity site is described by the same local Hamiltonian \mathcal{H}_i as in \mathcal{H}_{AIM} and therefore the interaction term remains local. On the other hand,

the hopping terms are now all short ranged with only nearest-neighbor hopping t_l . Therefore, the model described by \mathcal{H} is a simple one-dimensional system of L sites, as schematically shown in Fig. 1(b), and can be best treated by the DMRG method [20, 21, 28, 29].

Four remarks are in order regarding the method introduced here. First, as it is well known in the standard Lanczos method [27], the transformation from \mathcal{H}_r to \mathcal{H} is exact only when $L = 2M + 1$, assuming that \mathbf{p}_1 is not contained in an invariant subspace and thus the Lanczos iteration is not terminated before generating \mathbf{p}_{2M+1} . Only in this case, $(\hat{P}\hat{P}^T)_{k,k'} = \delta_{k,k'}$ and thus

$$\mathbf{a}_\sigma^\dagger \hat{H}_0 \mathbf{a}_\sigma = \mathbf{a}_\sigma^\dagger \hat{P} \hat{P}^T \hat{H}_0 \hat{P} \hat{P}^T \mathbf{a}_\sigma = \mathbf{f}_\sigma^\dagger \hat{H}'_0 \mathbf{f}_\sigma \quad (21)$$

as \hat{P} is a $(2M + 1) \times (2M + 1)$ orthogonal matrix.

Second, it is apparent from the construction that this method is for calculations in the thermodynamic limit. M and also Λ in the logarithmic discretization scheme determine the energy resolution as well as the model parameters ε_l and t_l in \mathcal{H} . Therefore, these quantities M and Λ control the accuracy of \mathcal{H} with respect to \mathcal{H}_{AIM} in the thermodynamic limit. In principle, the logarithmic discretization scheme becomes exact when $\Lambda \rightarrow 1 + 0^+ (= 1^+)$ and $M \rightarrow \infty$, where 0^+ is positive infinitesimal. Similarly, the constant discretization scheme becomes exact when $M \rightarrow \infty$. However, as discussed in Appendix B, we find that reasonably large M and L (but $L \leq 2M + 1$) can well represent the thermodynamic limit (provided that Λ is sufficiently small for the logarithmic discretization scheme).

Third, the single-impurity Anderson model in two spatial dimensions is considered here. This is only to simplify the explanation of the method introduced here. The extension of the method to more general cases such as a two-impurity Anderson model and a multiorbital many-impurity Anderson model is rather straightforward by using the block Lanczos technique [30]. Indeed, the similar transformation for Anderson impurity models in real space and its extension to multiorbital systems are found in Refs. [30–32]. The extension to three-dimensional systems is also straightforward.

Fourth, the method is similar to the NRG approach [24] in that both treat Anderson impurity models represented in energy space. Indeed, the logarithmic discretization scheme is employed in the NRG method, where M corresponds to the number of renormalization iterations [24]. However, these two approaches are conceptually different because the DMRG method optimizes the wave function based on the largest eigenstates of the reduced density matrix for that wave function, while the NRG method constructs the low-energy effective Hamiltonian based on the lowest eigenstates of the Hamiltonian. Note also that the method introduced here can take into account the band structure effect accurately over large energy scales, in contrast to the low-energy approximate approaches. This is obviously important when high-energy excitations are discussed.

C. Pseudogap Anderson model

It is valuable to compare the results for the single-impurity Anderson model on the honeycomb lattice with those for the corresponding pseudogap Anderson model. The pseudogap Anderson model is described by Hamiltonian \mathcal{H}_ω or \mathcal{H}_r with the following local density of states $\rho_{\text{PGA}}(\omega)$ per spin for the conduction band (see Fig. 2):

$$\rho_{\text{PGA}}(\omega) = \begin{cases} 4|\omega|/W^2 & \text{for } |\omega| \leq W/2, \\ 0 & \text{for } |\omega| > W/2. \end{cases} \quad (22)$$

This local density of states is directly used for $\rho(\omega)$ in Eqs. (5) and (7) to construct \mathcal{H} , which then can be solved by the DMRG method, as described above. The asymptotic behavior of $\rho(\omega)$ for the conduction band on the honeycomb lattice described by \mathcal{H}_c is

$$\rho(\omega) \sim \frac{1}{\sqrt{3}\pi t^2} |\omega| \quad (23)$$

for ω around zero [3]. Therefore, by setting the band width W for the pseudogap Anderson model as $W^2 = 4\sqrt{3}\pi t^2$, $\rho_{\text{PGA}}(\omega)$ can reproduce exactly the asymptotic behavior of $\rho(\omega)$ for the conduction band on the honeycomb lattice, as shown in Fig. 2.

The pseudogap Anderson model and its strong coupling counterpart, i.e., the pseudogap Kondo model, have been studied extensively using the analytical and NRG methods [4–11]. The ground-state phase diagram of the pseudogap Anderson model has two distinct phases, the LM phase and the ASC phase, and the VF point at the phase boundary [7]. In the LM phase, a free local moment at the impurity site survives without Kondo screening even at zero temperature. The fixed point of this phase can be characterized as $(\varepsilon, U, V) \rightarrow (\varepsilon^*, U^*, V^*) = (\varepsilon^*, 2\varepsilon^*, 0)$ with $\varepsilon^* = \infty$ [7], i.e., the free local moment being decoupled from the conduction band. In the ASC phase, the fixed point is characterized as $(\varepsilon^*, U^*, V^*) = (\infty, 0, 0)$ for $\varepsilon > U/2$, and $(\varepsilon^*, U^*, V^*) = (-\infty, 0, 0)$ for $\varepsilon < U/2$ [7]. Since the two electrons (two holes) occupy the impurity site for $\varepsilon > U/2$ ($\varepsilon < U/2$), no local moment is formed. The fixed point for the VF point is characterized as $(\varepsilon^*, U^*, V^*) = (0, \infty, 0)$ for $\varepsilon < U/2$ and $(\varepsilon^*, U^*, V^*) = (\varepsilon^*, \varepsilon^*, 0)$ with $\varepsilon^* = \infty$ for $\varepsilon > U/2$ [7]. Since the impurity site is decoupled from the conduction band, the ground state is threefold degenerate due to three different local states at the impurity site, i.e., the empty state and the singly occupied states with up or down electron for $\varepsilon < U/2$.

III. RESULTS

We first summarize briefly the conditions employed for the numerical calculations before discussing the numerical results for the single-impurity Anderson model on the honeycomb lattice. These results are then compared with those for the pseudogap Anderson model. We also

examine the entanglement spectrum for the ground state of the single-impurity Anderson model on the honeycomb lattice to characterize the impurity quantum phase transition.

A. Numerical details

We set that $L = M$ (even) in Eq. (20) throughout the calculations discussed here, unless otherwise stated. As already explained in Sec. II B, M (and also Λ when the logarithmic discretization scheme is used) controls the energy resolution and L can be taken to be up to $2M + 1$. Therefore, in principle, one should take the infinite limit of M and L along with $\Lambda \rightarrow 1^+$ for the logarithmic discretization scheme. However, we find that the quantities studied here are well converged for sufficiently large but finite values of M and L with keeping a fixed ratio of L/M , at least, when the logarithmic discretization scheme with Λ as small as 1.15 is used (see Appendix B). Therefore, we take $L (= M)$ up to 128 with the z component of total spin $S_z = 0$ and keep $m_D \sim 32L$ largest eigenstates of the reduced density matrix in the DMRG calculations.

When the logarithmic discretization scheme is used, the discarded weights are found to be significantly small, typically of the order 10^{-13} – 10^{-11} . The corresponding error of the ground-state energy is as small as $\sim 10^{-8}t$, which is even smaller than the smallest level spacing of the eigenvalues for \hat{H}'_0 in Eq. (18) with $L = M$. When the constant discretization scheme is used, the discarded weights are as small as 10^{-9} and the corresponding error of the ground-state energy is about $10^{-7}t$. We employ the logarithmic discretization scheme to calculate the static quantities as well as the entanglement spectrum and the constant discretization scheme to calculate the full excitation spectra (see Appendix B). However, to extrapolate the static limit of the dynamical quantity, we use the logarithmic discretization scheme with m_D up to $48L$. It should be also noted that the ground state is found to be always singlet as long as L is even and finite.

B. Local static quantities

Let us first calculate the local density per spin at the impurity site

$$\bar{n}_{i\sigma} = \langle \psi_0 | n_{i\sigma} | \psi_0 \rangle \quad (24)$$

and the total spin at the impurity site

$$\bar{S}_i = \langle \psi_0 | \vec{S}_i \cdot \vec{S}_i | \psi_0 \rangle, \quad (25)$$

where $|\psi_0\rangle$ is the ground state and the spin operator \vec{S}_i at the impurity site is given as

$$\vec{S}_i = \frac{1}{2} \sum_{\sigma_1, \sigma_2} c_{i, \sigma_1}^\dagger \vec{\tau}_{\sigma_1, \sigma_2} c_{i, \sigma_2} \quad (26)$$

with $\vec{\tau} = (\tau_x, \tau_y, \tau_z)$ being Pauli matrices. Note that $\bar{n}_{i\uparrow} = \bar{n}_{i\downarrow}$ because of $SU(2)$ symmetry of \mathcal{H} and $\bar{S}_i \leq 0.75$.

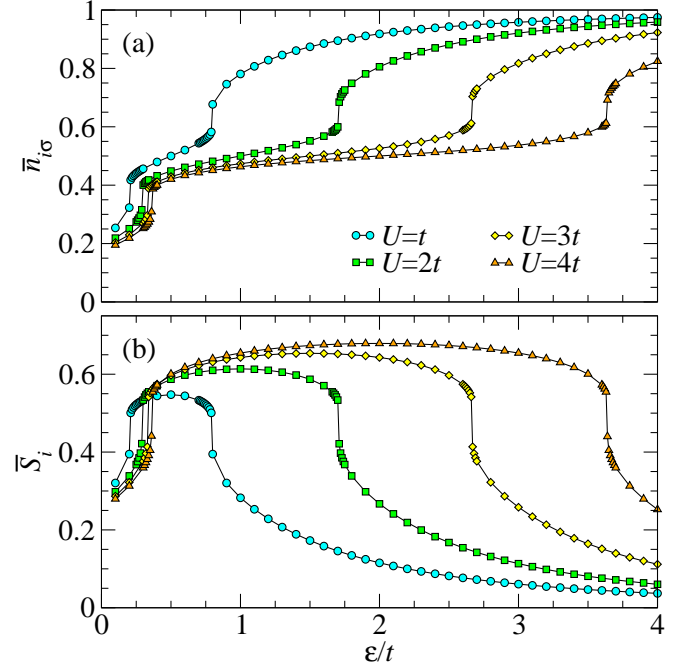


FIG. 3. (Color online) (a) Local density $\bar{n}_{i\sigma}$ and (b) total spin \bar{S}_i at the impurity site for the single-impurity Anderson model on the honeycomb lattice as a function of ϵ with $V = t$ and various U indicated in (a). The logarithmic discretization scheme with $\Lambda = 1.15$ and $M = 128$ is used.

As shown in Fig. 3, we find that these quantities change discontinuously at two distinct values of ϵ for given U and V . It should be emphasized, however, that these deceptively discontinuous changes are simply due to a finite grid size of ϵ used in the figures, but not due to the level crossing of two different states as often found in finite-size calculations. Indeed, we find in Fig. 4 that these quantities vary smoothly with ϵ when a much smaller grid size of ϵ is used. We also find in Fig. 4 that the change of these quantities becomes sharper and steeper with increasing M . Therefore, we expect that it becomes truly discontinuous only when we take the limit of $M \rightarrow \infty$.

Nevertheless, the steep changes of these quantities imply that there are three phases for a given U , a low-density phase ($\bar{n}_{i\sigma} \lesssim 0.3$) for small ϵ , an intermediate density phase ($\bar{n}_{i\sigma} \sim 0.5$) which includes the particle-hole symmetric limit with $\epsilon = U/2$, and a high-density phase ($\bar{n}_{i\sigma} \gtrsim 0.7$) for large ϵ . While the total spin \bar{S}_i is suppressed in the low- and high-density phases, it is enhanced in the intermediate density phase. It should be noticed here that the low- and high-density phases are related under the particle-hole transformation. This is because the model with a parameter set (ϵ, U, V) in particle picture can be transformed into the same model with $(U - \epsilon, U, V)$ in hole picture. Indeed, our results satisfy that $\bar{n}_{i\sigma}$ (\bar{S}_i) at the impurity potential ϵ is exactly the

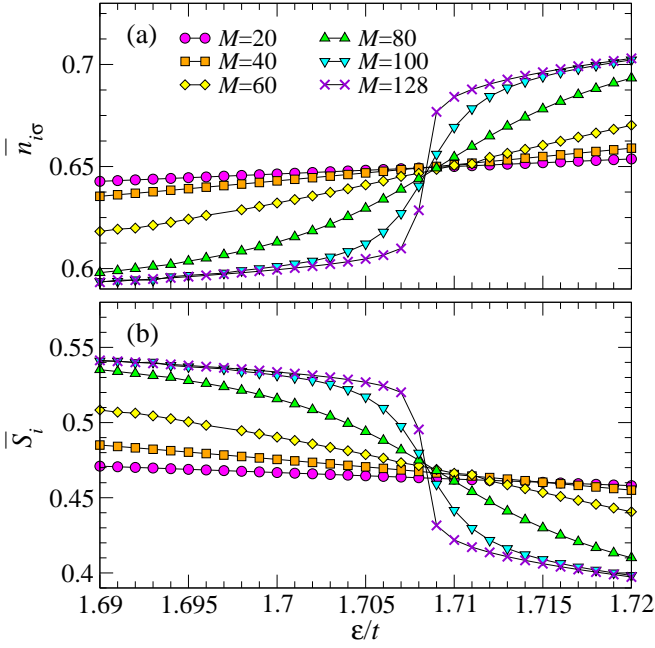


FIG. 4. (Color online) Same as in Fig. 3 but with $U = 2t$ and a finer grid size of ε for different values of M indicated in (a).

same as $1 - \bar{n}_{i\sigma}$ (\bar{S}_i) at the impurity potential $U - \varepsilon$ for given U and V . Together with the results of the spin and charge excitation spectra shown in Sec. III C, we identify the intermediate density phase as the LM phase where the local moment is formed at the impurity site, and the low- and high-density phases as the ASC phase where essentially two holes or electrons occupy the impurity site with no local moment formed.

C. Ground-state phase diagram

Systematically calculating $\bar{n}_{i\sigma}$ and \bar{S}_i for different values of V , we obtain the ground-state phase diagram for the single-impurity Anderson model on the honeycomb lattice in a wide range of parameters, ε and U . As shown in Fig. 5, the LM phase appears around the particle-hole symmetric limit with $\varepsilon = U/2$, where $\bar{n}_{i\sigma}$ is exactly 1/2. The region of this phase is found to decrease with increasing V . This is easily understood by considering that the increase of V enhances the bonding between the impurity site and the conduction site \mathbf{r}_0 , which then leads to the formation of the bond singlet state. Eventually, the LM phase exists only along the particle-hole symmetric line in the limit of $V \rightarrow \infty$. Our results in Fig. 5 also imply the absence of Kondo screening phase. This can be understood simply as the consequence of the characteristic density of states of the conduction band since the Kondo temperature $T_K \sim \sqrt{UV^2\rho(0)/2}\exp[-\pi|(U-\varepsilon)|/4UV^2\rho(0)]$ [33]. The phase diagram is therefore in good qualitative agree-

ment with that obtained by the low-energy approximate approaches [6, 7]. In fact, as discussed below in Sec. III E, the phase diagram is found to be quantitatively compared with that for the pseudogap Anderson model.

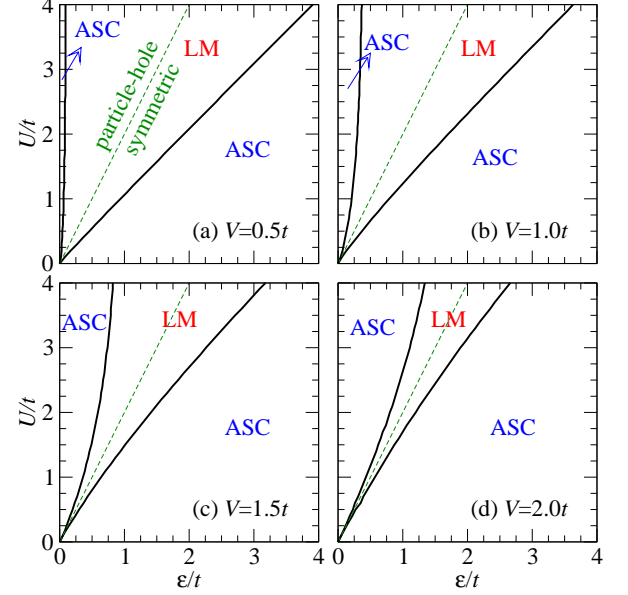


FIG. 5. (Color online) Ground-state phase diagrams for the single-impurity Anderson model on the honeycomb lattice in a wide range of parameters, ε and U , with four different values of V indicated in the figures. LM (ASC) stands for the local moment (asymmetric strong coupling) phase. The particle-hole symmetric line $\varepsilon = U/2$ is indicated by green dashed lines. The phase boundaries are determined by the calculations of the static quantities shown in Fig. 3.

D. Dynamical quantities

Next, we calculate the dynamical quantities to support the assignment of different phases found in the phase diagram. The dynamical quantities studied here are the spin excitation spectrum at impurity site

$$\chi_s(\omega) = -\frac{1}{\pi} \text{Im} \langle \psi_0 | S_i^z \frac{1}{\omega + i\eta - \mathcal{H} + E_0} S_i^z | \psi_0 \rangle \quad (27)$$

and the charge excitation spectrum at impurity site

$$\chi_c(\omega) = -\frac{1}{\pi} \text{Im} \langle \psi_0 | n_i \frac{1}{\omega + i\eta - \mathcal{H} + E_0} n_i | \psi_0 \rangle, \quad (28)$$

where E_0 is the ground-state energy and η is a broadening factor. We calculate these quantities using the dynamical DMRG method [34].

Figure 6 shows the spin excitation spectra $\chi_s(\omega)$ for $V = t$ and $U = 2t$. In this case, the transition occurs at $\varepsilon = \varepsilon_c \sim 1.707t - 1.708t$. As seen in Fig. 6, $\chi_s(\omega)$ in the LM phase for $\varepsilon < \varepsilon_c$ increases as $\omega \rightarrow 0$. In contrast, $\chi_s(\omega)$ for $\omega \rightarrow 0$ is suppressed in the ASC phase for $\varepsilon > \varepsilon_c$. The M dependence of $\chi_s(0)$ shown in the inset of

Fig. 6 reveals that $\chi_s(0)$ in the LM (ASC) phase increases (decreases) exponentially with M for large M , i.e.,

$$\chi_s(0) \propto \exp(\tau_s M) \quad (29)$$

with the same τ_s in each phase, independent of values of ε , as summarized in Table I. Therefore, we can safely conclude that

$$\lim_{M \rightarrow \infty} \chi_s(0) \rightarrow \infty \quad (30)$$

in the LM phase and

$$\lim_{M \rightarrow \infty} \chi_s(0) \rightarrow 0 \quad (31)$$

in the ASC phase. The divergent behavior of $\chi_s(0)$ implies the presence of free local moment in the LM phases, while $\chi_s(0) = 0$ indicates no local moment at the impurity site in the ASC phase.

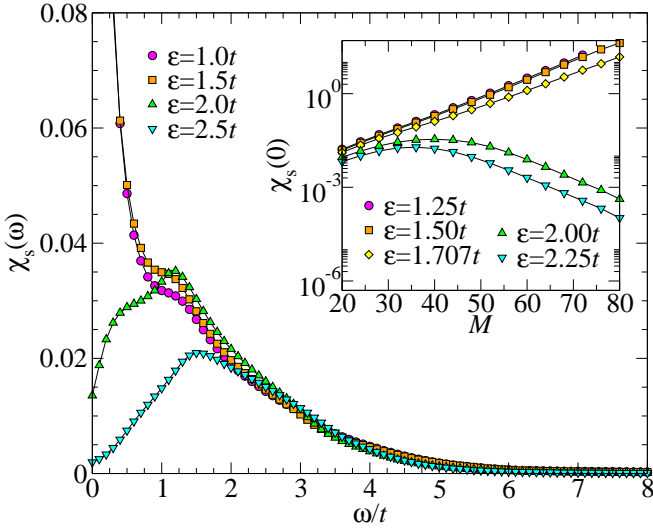


FIG. 6. (Color online) Spin excitation spectra $\chi_s(\omega)$ at the impurity site for the single-impurity Anderson model on the honeycomb lattice with $V = t$ and $U = 2t$. The constant discretization scheme with $M = 100$ is used and a broadening factor of $\eta = 0.2t$ is set. The inset shows the M dependence of $\chi_s(0)$ calculated using the logarithmic discretization scheme with $\Lambda = 1.15$ and $\eta = 25W\Lambda^{-M}$.

TABLE I. The diverging or decaying factors τ_s and τ_c of the local spin and charge excitation spectra at $\omega = 0$, $\chi_s(0) \propto \exp(\tau_s M)$, and $\chi_c(0) \propto \exp(\tau_c M)$, respectively, for large M in the three different regions of the phase diagram, i.e., the LM and ASC phases and the VF point, estimated from the results shown in Figs. 6 and 7.

	LM phase	ASC phase	VF point
τ_s	0.140	-0.140	0.123
τ_c	-0.143	-0.142	0.082

The charge excitation spectra $\chi_c(\omega)$ are shown in Fig. 7. In contrast to $\chi_s(\omega)$, we find that $\chi_c(\omega) \rightarrow 0$

for $\omega \rightarrow 0$ in both LM and ASC phases. This is more apparent in the M dependence of $\chi_c(0)$, as shown in the inset of Fig. 7, because for large M

$$\chi_c(0) \propto \exp(\tau_c M) \quad (32)$$

with $\tau_c < 0$ (also see Table I), and thus

$$\lim_{M \rightarrow \infty} \chi_c(0) \rightarrow 0 \quad (33)$$

in the LM and ASC phases. However, for the exact phase boundary at $\varepsilon = \varepsilon_c$, we find that $\chi_s(0)$ as well as $\chi_c(0)$ increases exponentially with M (see the insets of Figs. 6 and 7, and also see Table I), and therefore

$$\lim_{M \rightarrow \infty} \chi_s(0) \rightarrow \infty \quad (34)$$

and

$$\lim_{M \rightarrow \infty} \chi_c(0) \rightarrow \infty, \quad (35)$$

suggesting the VF point. In the renormalization group analysis, the VF fixed point is characterized by the renormalized parameters $(\varepsilon^*, U^*, V^*) = (0, \infty, 0)$ for $\varepsilon < U/2$ [7]. Consequently, three local states at the impurity site, $|0\rangle_i$, $|\uparrow\rangle_i$, and $|\downarrow\rangle_i$, contribute equally to the threefold-degenerate ground state and thus both $\chi_s(0)$ and $\chi_c(0)$ diverge.

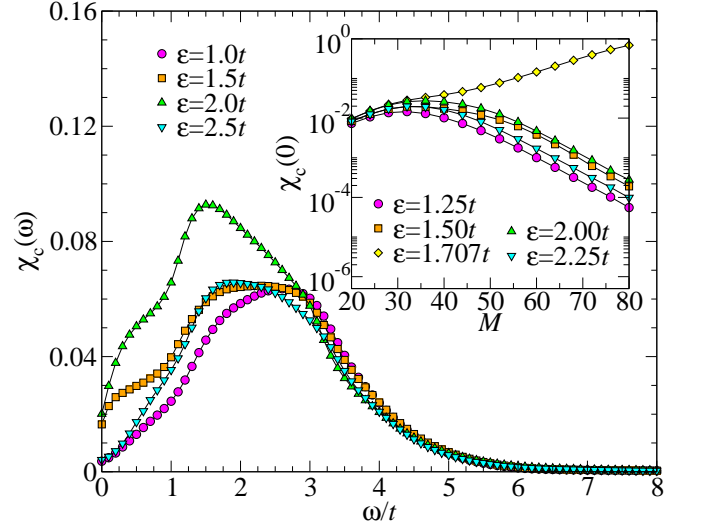


FIG. 7. (Color online) Charge excitation spectra $\chi_c(\omega)$ at the impurity site for the single-impurity Anderson model on the honeycomb lattice with $V = t$ and $U = 2t$. The constant discretization scheme with $M = 100$ is used and a broadening factor of $\eta = 0.2t$ is set. The inset shows the M dependence of $\chi_c(0)$ calculated using the logarithmic discretization scheme with $\Lambda = 1.15$ and $\eta = 25W\Lambda^{-M}$.

E. Results for the pseudogap Anderson model

Here, we compare the results of the local static quantities, the ground-state phase diagram, and the excitation

spectra for the pseudogap Anderson model at half-filling, i.e., $n = 1$, to those for the single-impurity Anderson model on the honeycomb lattice discussed above.

Figure 8 shows the local density $\bar{n}_{i\sigma}$ and total spin \bar{S}_i at the impurity site for the pseudogap Anderson model. We find in Fig. 8 that these local static quantities, including the phase boundaries where the abrupt changes of these quantities occur, for the pseudogap Anderson model are in quantitatively excellent agreement with those for the single-impurity Anderson model on the honeycomb lattice. Since the pseudogap Anderson model is a low-energy effective model for the single-impurity Anderson model on the honeycomb lattice, our results ensure that the low-energy effective description of the pseudogap Anderson model is quantitatively valid for these static quantities.

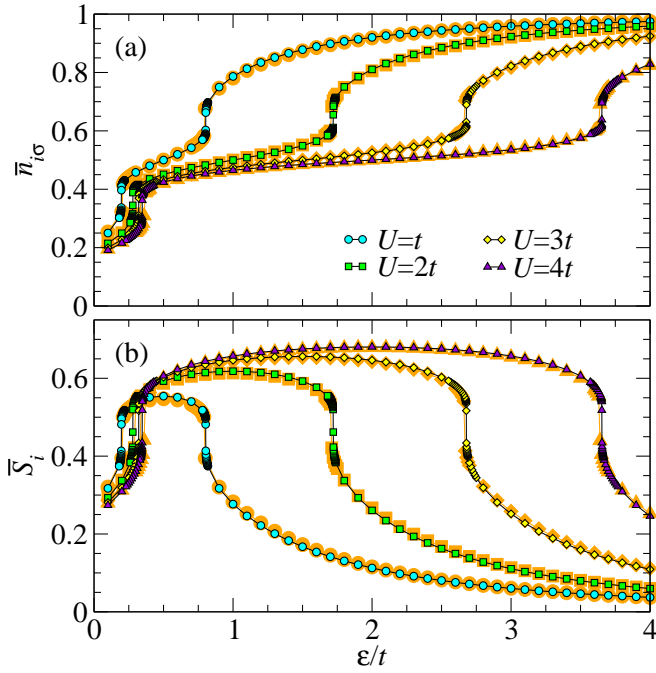


FIG. 8. (Color online) (a) Local density $\bar{n}_{i\sigma}$ and (b) total spin \bar{S}_i at the impurity site for the pseudogap Anderson model as a function of ϵ with $V = t$ and various U indicated in (a). The logarithmic discretization scheme with $\Lambda = 1.15$ and $M = 128$ is used. For comparison, the results for the single-impurity Anderson model on the honeycomb lattice shown in Fig. 3 are also indicated by orange shaded symbols.

Systematically calculating $\bar{n}_{i\sigma}$ and \bar{S}_i for different values of V , we obtain in Fig. 9 the ground-state phase diagram for the pseudogap Anderson model. We find that the phase boundaries are almost identical to those for the single-impurity Anderson model on the honeycomb lattice. For instance, the VF point for $V = t$ and $U = 2t$ is located at $\epsilon_c = 1.721t$ – $1.722t$ for the pseudogap Anderson model, which is comparable with $\epsilon_c = 1.707t$ – $1.708t$ for the single-impurity Anderson model on the honeycomb lattice.

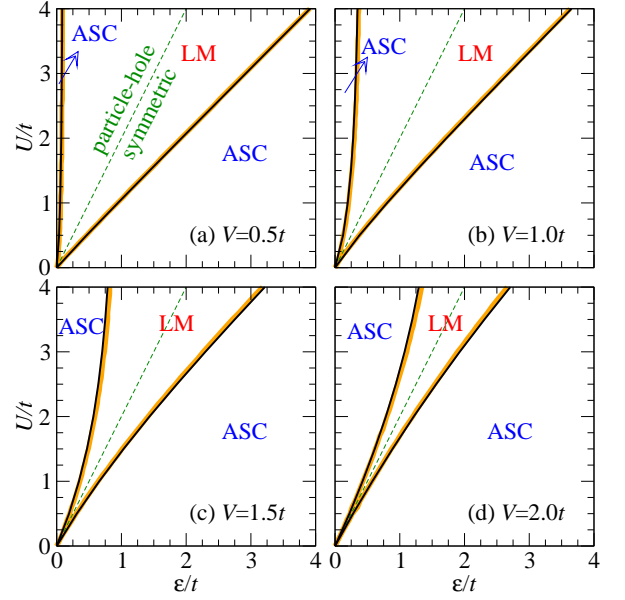


FIG. 9. (Color online) Ground-state phase diagrams for the pseudogap Anderson model in a wide range of parameters, ϵ and U , with four different values of V indicated in the figures. LM (ASC) stands for the local moment (asymmetric strong coupling) phase. The particle-hole symmetric line $\epsilon = U/2$ is indicated by green dashed lines. The phase boundaries (black solid lines) are determined by the calculations of the static quantities shown in Fig. 8. For comparison, the phase boundaries for the single-impurity Anderson model on the honeycomb lattice are also indicated by orange bold lines.

Figures 10 and 11 show the spin and charge excitation spectra at the impurity site, $\chi_s(\omega)$ and $\chi_c(\omega)$, respectively. Comparing with Figs. 6 and 7, the line shapes of these excitation spectra are apparently different from those for the single-impurity Anderson model on the honeycomb lattice. However, as shown in the insets of Figs. 10 and 11, we find that the asymptotic behavior of these quantities around $\omega \sim 0$ are qualitatively the same for both models, i.e., $\chi_s(0) \rightarrow \infty$ and $\chi_c(0) \rightarrow 0$ in the LM phase, $\chi_s(0) \rightarrow 0$ and $\chi_c(0) \rightarrow 0$ in the ASC phase, and $\chi_s(0) \rightarrow \infty$ and $\chi_c(0) \rightarrow \infty$ at the VF point. Assuming that $\chi_s(0)$ and $\chi_c(0)$ diverge or decay exponentially for large M , as in Eqs. (29) and (32), we can estimate the diverging or decaying factors τ_s and τ_c for the pseudogap Anderson model. As shown in Table II, we find that the obtained τ_s and τ_c are indeed very close to those for the single-impurity Anderson model on the honeycomb lattice shown in Table I, indicating that the asymptotically low-energy excitations of the single-impurity Anderson model on the honeycomb lattice are also well described by the low-energy effective pseudogap Anderson model.

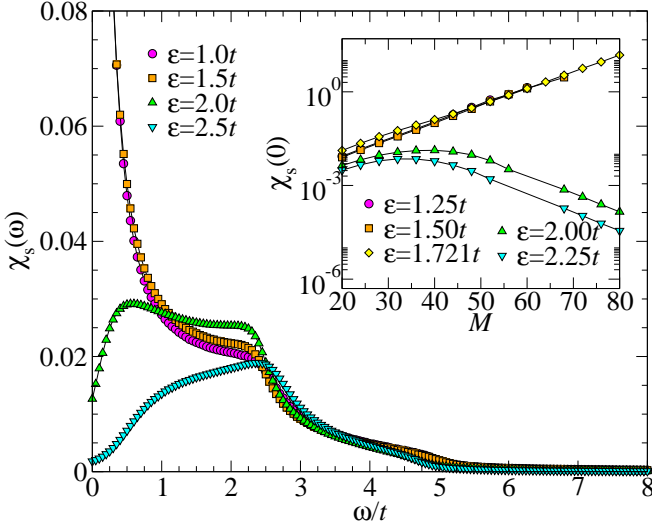


FIG. 10. (Color online) Spin excitation spectra $\chi_s(\omega)$ at the impurity site for the pseudogap Anderson model with $V = t$ and $U = 2t$. The constant discretization scheme with $M = 100$ is used and a broadening factor of $\eta = 0.2t$ is set. The inset shows the M dependence of $\chi_s(0)$ calculated using the logarithmic discretization scheme with $\Lambda = 1.15$ and $\eta = 25W\Lambda^{-M}$.

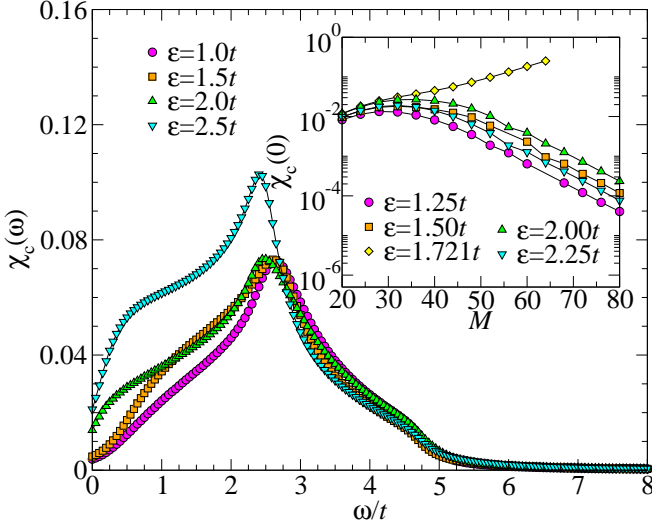


FIG. 11. (Color online) Charge excitation spectra $\chi_c(\omega)$ at the impurity site for the pseudogap Anderson model with $V = t$ and $U = 2t$. The constant discretization scheme with $M = 100$ is used and a broadening factor of $\eta = 0.2t$ is set. The inset shows the M dependence of $\chi_c(0)$ calculated using the logarithmic discretization scheme with $\Lambda = 1.15$ and $\eta = 25W\Lambda^{-M}$.

F. Entanglement spectrum

Let us now discuss the entanglement spectrum for the ground state of the single impurity Anderson model on the honeycomb lattice. In the DMRG method, the system is divided into two parts, the left and right blocks,

TABLE II. The diverging or decaying factors τ_s and τ_c of the local spin and charge excitation spectra at $\omega = 0$, $\chi_s(0) \propto \exp(\tau_s M)$ and $\chi_c(0) \propto \exp(\tau_c M)$, respectively, for large M in the three different regions of the phase diagram, i.e., the LM and ASC phases and the VF point, estimated from the results shown in Figs. 10 and 11.

	LM phase	ASC phase	VF point
τ_s	0.132	-0.140	0.115
τ_c	-0.140	-0.140	0.079

as shown in Fig. 1(b), with the sizes being l_L and l_R , respectively, i.e., $L = l_L + l_R$. Thus, the wave function is generally represented as

$$|\psi\rangle = \sum_i \sum_j \psi_{i,j} |i\rangle_L \otimes |j\rangle_R, \quad (36)$$

where $|i\rangle_L$ and $|j\rangle_R$ indicate the bases of the left and right blocks, respectively. The reduced density matrix $\hat{\rho}_L$ for the left block is

$$(\hat{\rho}_L)_{i,i'} = \sum_j \psi_{i,j} \psi_{i',j}^*, \quad (37)$$

and the k th eigenvalue of $\hat{\rho}_L$ is denoted as λ_k in descending order, i.e.,

$$\lambda_1 \geq \lambda_2 \geq \dots \geq \lambda_{m_D}, \quad (38)$$

where m_D is the number of density matrix eigenstates kept in the DMRG calculations. One can readily show that $0 \leq \lambda_k \leq 1$ and $\sum_k \lambda_k = 1$ when $\langle \psi | \psi \rangle = 1$. The entanglement spectrum ξ_k [12] is defined as

$$\xi_k = -\ln \lambda_k, \quad (39)$$

and hence

$$\xi_1 \leq \xi_2 \leq \dots \leq \xi_{m_D}. \quad (40)$$

Figure 12 shows a low-lying part of ξ_k for the ground state at the vicinity of the phase boundary. It is clear in Fig. 12(a) that the lowest and the first excited entanglement levels cross at $\varepsilon = \varepsilon_c$. As shown in Fig. 12(b), we find that the lowest entanglement level for l_L odd is doubly degenerate in the LM phase, singlet in the ASC phase, and accidentally three fold degenerate at $\varepsilon = \varepsilon_c$, i.e., the VF point [35]. Because of the qualitatively different behavior, we can consider the gap of the entanglement spectrum

$$\Delta\xi = \xi_2 - \xi_1 \quad (41)$$

as an “order parameter” to distinguish the different phases in the phase diagram. As shown in Fig. 12(c), $\Delta\xi$ changes abruptly at $\varepsilon = \varepsilon_c$ for large M and it is finite only when $\varepsilon > \varepsilon_c$. Indeed, the phase boundary determined from ξ_k is the same as the one estimated in Fig. 3. This clearly demonstrates that $\Delta\xi$ serves as a quantity to determine the phase boundary of the impurity quantum phase transition. We should emphasize

here that the ground state is always singlet as long as L is even and finite. Therefore, the similar characteristic feature of the degeneracy in the low-lying entanglement spectrum is absent in the low-lying energy spectrum.

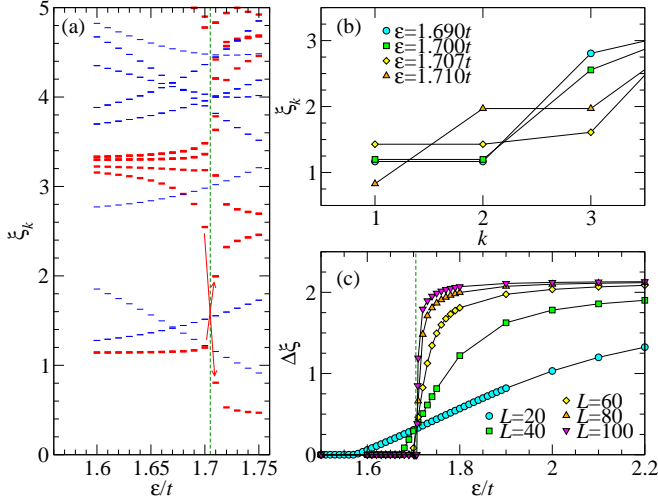


FIG. 12. (Color online) Entanglement spectrum for the ground state of the single-impurity Anderson model on the honeycomb lattice with $V = t$ and $U = 2t$. The logarithmic discretization scheme with $\Lambda = 1.15$ is used. (a) Low-lying entanglement spectrum ξ_k (red bars) for ε at the vicinity of the phase boundary $\varepsilon_c \sim 1.707t-1.708t$ (dashed vertical line) determined in Fig. 3. The calculations are for $L = 100$ with the left block size $l_L = 51$. For comparison, the results for $L = 40$ with $l_L = 21$ are also shown by blue bars, in which the phase boundary is approximately $1.67t$. Red arrows are guide for eyes. (b) The lowest three levels of ξ_k for ε close to ε_c , calculated for $L = 100$ with $l_L = 51$. (c) Gap of the entanglement spectrum, $\Delta\xi \sim \xi_2 - \xi_1$, as a function of ε for various L with $l_L = L/2 + 1$. The phase boundary ε_c determined in Fig. 3 is indicated by a dashed vertical line.

Let us now discuss the intuitive understanding of the origin for the different degeneracy of the low-lying entanglement spectrum ξ_k in each phase. We first note that in our calculations the impurity site is located at the left edge [see Fig. 1(b)] and the degeneracy of the lowest entanglement level in the LM phase occurs only for l_L odd. This implies that the degeneracy in the LM phase is due to the quantum number conservation in each block. Clearly, the ground state of the LM phase is doubly degenerate in $L \rightarrow \infty$ and is described schematically as $|\psi_1\rangle \sim |\uparrow\rangle_L \otimes |\downarrow\rangle_R$ and $|\psi_2\rangle \sim |\downarrow\rangle_L \otimes |\uparrow\rangle_R$, where $s = \uparrow, \downarrow$, and 0 in $|s\rangle_{L(R)}$ indicates the z component of total spin $S_z = 1/2, -1/2$, and 0, respectively, in the left (right) block of the ground state. Here, nonzero s in $|s\rangle_L$ is due to the localized spin formed around the impurity site, and correspondingly $|s\rangle_R$ has the opposite spin to compensate the spin in the left block [see Figs. 13(a) and 13(b)]. In a finite L , however, these two states $|\psi_1\rangle$ and $|\psi_2\rangle$ are entangled and the ground state is $|\psi_0\rangle \sim (|\psi_1\rangle - |\psi_2\rangle)/\sqrt{2}$. We can now readily show that the lowest ξ_k is doubly degenerate. This is no longer the case when l_L is even.

Although the impurity site is still represented approximately as $|\uparrow\rangle_i$ or $|\downarrow\rangle_i$, $|s\rangle_L \sim |0\rangle_L$ for l_L even because $|\uparrow\rangle_i$ and $|\downarrow\rangle_i$ must be entangled in the left block due to the conservation of S_z [36]. Therefore, the lowest ξ_k is no longer degenerate when l_L is even.

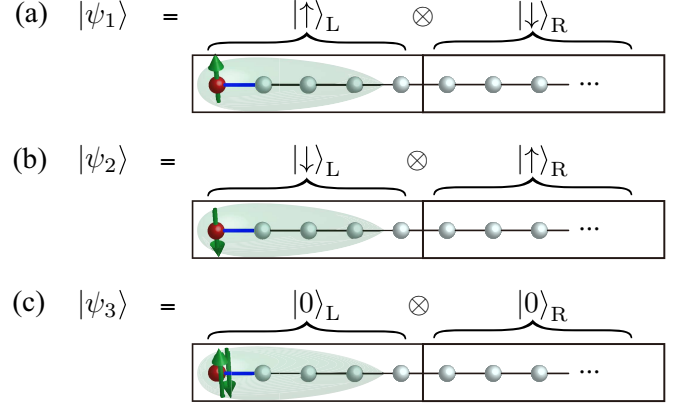


FIG. 13. (Color online) (a) One of the doubly degenerate ground states for $L \rightarrow \infty$, $|\psi_1\rangle$, in the LM phase. (b) The other state, $|\psi_2\rangle$, of the doubly degenerate ground states in the LM phase. (c) The singlet ground state $|\psi_3\rangle$ in the ASC phase. Here, $s = \uparrow, \downarrow$, and 0 in $|s\rangle_{L(R)}$ represents the z component of total spin $S_z = 1/2, -1/2$, and 0, respectively, in the left (right) block of $|\psi_i\rangle$ for $i = 1, 2$, and 3. Red spheres at the left edge represent the impurity site and green arrows indicate the local spin configurations around the impurity site which may be spatially extended into the green shaded region.

In the ASC phase for $\varepsilon > U/2$, the impurity site is approximately doubly occupied $|\uparrow\downarrow\rangle_i$. Therefore, the ground state is described as $|\psi_3\rangle \sim |0\rangle_L \otimes |0\rangle_R$, as schematically shown in Fig. 13(c), and thus the lowest ξ_k is not degenerate [37]. The VF point, on the other hand, corresponds to the special case where $|\psi_1\rangle$, $|\psi_2\rangle$, and $|\psi_3\rangle$ are all degenerate in $L \rightarrow \infty$. These three states are entangled in a finite L and the ground state is represented approximately as $|\psi_0\rangle \sim (|\psi_1\rangle - |\psi_2\rangle + |\psi_3\rangle)/\sqrt{3}$. We can now show that the lowest ξ_k for $|\psi_0\rangle$ is three fold degenerate.

Finally, let us briefly discuss the l_L dependence of the entanglement spectrum gap $\Delta\xi$ and the entanglement entropy S_E . The entanglement entropy is a quantity to measure the degree of quantum entanglement between the left and right blocks of a given quantum state $|\psi\rangle$ and is defined as

$$S_E = -\text{Tr} \hat{\rho}_L \ln \hat{\rho}_L = -\sum_{k=1}^{m_D} \lambda_k \ln \lambda_k. \quad (42)$$

Fig. 14 shows the l_L dependence of these quantities calculated for the ground state of the single-impurity Anderson model on the honeycomb lattice.

Because the degeneracy of the lowest entanglement level, i.e., the largest λ_k , is different in each region of the phase diagram, we find in Fig. 14(b) that S_E can exhibit a maximum around the phase boundary when l_L is

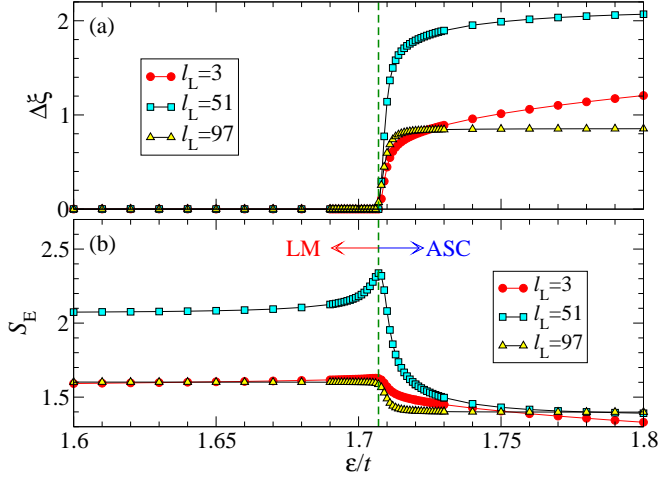


FIG. 14. (Color online) (a) Entanglement spectrum gap $\Delta\xi$ and (b) entanglement entropy S_E for the ground state of the single-impurity Anderson model on the honeycomb lattice with $V = t$ and $U = 2t$. The calculations are for $L = 100$ with three different l_L indicated in the figures. The logarithmic discretization scheme with $\Lambda = 1.15$ and $M = 100$ is used. Green dashed lines indicate the phase boundary ε_c determined in Fig. 3.

chosen appropriately. Therefore, S_E can also be an indicator to estimate the transition point of the impurity quantum phase transition. However, in contrast to $\Delta\xi$, the variation of S_E is rather smooth across the transition for a finite L . Furthermore, we find that S_E can even monotonically decrease with increasing ε without showing a peak structure around the transition point [see, for example, the results for $l_L = 97$ in Fig. 14(b)]. This indicates that the maximum of S_E is not always located at the phase boundary. Thus, the degeneracy of the low-lying entanglement spectrum is a much better quantity to determine the phase boundary for the finite- L calculations.

IV. SUMMARY

We have introduced the DMRG method in energy space for Anderson impurity models, which allows us for calculations in the thermodynamic limit. We have applied this method to the single-impurity Anderson model on the honeycomb lattice to establish the ground-state phase diagram at half-filling. By systematically calculating the local static quantities, we have found that the phase diagram contains two phases, i.e., the LM phase and the ASC phase, but no Kondo screening phase. To support these results, we have also calculated the spin and charge excitation spectra at the impurity site, which behave qualitatively differently in these phases and reveal the existence of the VF point at the phase boundary. These results are thus qualitatively in good agree-

ment with those obtained previously by the low-energy approximate approaches.

For quantitative comparison, we have also studied the low-energy effective pseudogap Anderson model using the method introduced here. Although the high-energy excitations are obviously different, we have found that the ground-state phase diagram and the asymptotic low-energy excitations are in good quantitative agreement with those for the single-impurity Anderson model on the honeycomb lattice. Therefore, our result provides the first quantitative justification for studies based on the low-energy effective models.

We have also discussed the entanglement properties for the ground state of the single-impurity Anderson model on the honeycomb lattice. We have found that the low-lying entanglement spectrum exhibits qualitatively different behaviors in the different regions of the phase diagram: the lowest entanglement level is doubly degenerate for the LM phase, singlet for the ASC phase, and three fold degenerate at the VF point. We have also provided the intuitive understanding of these different behaviors in the degeneracy of the lowest entanglement level. The degeneracy of the lowest entanglement level differs from the degeneracy of the lowest-energy level because the ground state is found to be always singlet as long as L is even and finite. Furthermore, we have shown that the entanglement entropy can exhibit a broad maximum around the phase transition point when the ground state is properly separated to calculate the entanglement entropy. However, this is not always the case and sometimes the entanglement entropy varies monotonically across the transition. Therefore, we conclude that the entanglement spectrum is a better quantity to distinguish different phases in the impurity quantum phase transition.

Finally, our present analysis has no intention to make the quantitative comparison with experiments on the impurity problem in graphene [1, 2]. For the quantitative comparison, further details not included in the simplest single-impurity Anderson model should be considered. For example, the electron correlation in the conduction band might have a significant effect on the nature of quasiparticles [38–42]. The incorporation of different chemical bondings between graphene and adatom inevitably requires more complex hybridization, which affects the local electronic and magnetic properties around the impurity [43]. Furthermore, the spin-orbit coupling induced by the structural deformation around the impurity can be significantly large [44–48]. A transition metal substrate can also induce a giant Rashba splitting in graphene [49, 50]. The method introduced here, in combination with the first-principles band-structure calculation based on the density functional theory, would be a valuable extension to disentangle these effects for the impurity problem in graphene.

ACKNOWLEDGMENTS

The authors are grateful to K. Shinjo, R. Peters, E. Mnamitani, and H. Watanabe for valuable discussions. The computation has been done using the RIKEN Cluster of Clusters (RICC), the RIKEN supercomputer system (HOKUSAI GreatWave), and the facilities at Supercomputer Center in ISSP, Information Technology Center, University of Tokyo. This work has been supported by Grants-in-Aid for Scientific Research from JSPS under the Grants No. 24740269 and No. 26800171 and in part by RIKEN iTHES Project and Molecular Systems.

Appendix A: Effective actions of the impurity site for \mathcal{H}_{AIM} , \mathcal{H}_ω , and \mathcal{H}_r .

In this appendix, we show that the effective action of the impurity site for the single-impurity Anderson model \mathcal{H}_{AIM} on the honeycomb lattice is exactly the same as those for \mathcal{H}_ω and \mathcal{H}_r in energy space.

In the momentum space, \mathcal{H}_c and \mathcal{H}_V in \mathcal{H}_{AIM} are written, respectively, as

$$\mathcal{H}_c = \sum_{\mathbf{k}} \sum_{\sigma=\uparrow,\downarrow} \sum_{\zeta=\pm} \varepsilon_{\mathbf{k}}^{(\zeta)} c_{\mathbf{k},\zeta,\sigma}^\dagger c_{\mathbf{k},\zeta,\sigma} \quad (\text{A1})$$

and

$$\mathcal{H}_V = \frac{V}{\sqrt{2N}} \sum_{\mathbf{k}} \sum_{\sigma=\uparrow,\downarrow} \sum_{\zeta=\pm} e^{i\mathbf{k}\cdot\mathbf{r}_0} c_{i,\sigma}^\dagger c_{\mathbf{k},\zeta,\sigma} + \text{H.c.}, \quad (\text{A2})$$

where N is the number of unit cells and $c_{\mathbf{k},\zeta,\sigma}^\dagger$ ($c_{\mathbf{k},\zeta,\sigma}$) is an electron creation (annihilation) operator of the conduction band at momentum \mathbf{k} with the band dispersion

$$\varepsilon_{\mathbf{k}}^{(\zeta)} = \zeta t |1 + e^{i\mathbf{k}\cdot\mathbf{a}_1} + e^{i\mathbf{k}\cdot\mathbf{a}_2}|. \quad (\text{A3})$$

Here, \mathbf{a}_1 and \mathbf{a}_2 are the primitive lattice vectors of the honeycomb lattice. The partition function for \mathcal{H}_{AIM} is then

$$Z_{\text{AIM}} = \int \mathcal{D}\bar{\psi} \mathcal{D}\psi \exp[-S_{\text{AIM}}], \quad (\text{A4})$$

where

$$\begin{aligned} S_{\text{AIM}} = & \int_0^\beta d\tau \sum_{\sigma=\uparrow,\downarrow} \bar{\psi}_{i,\sigma}(\tau) (\partial_\tau - \varepsilon) \psi_{i,\sigma}(\tau) \\ & + \int_0^\beta d\tau \sum_{\mathbf{k}} \sum_{\sigma=\uparrow,\downarrow} \sum_{\zeta=\pm} \bar{\psi}_{\mathbf{k},\zeta,\sigma}(\tau) \partial_\tau \psi_{\mathbf{k},\zeta,\sigma}(\tau) \\ & + \int_0^\beta d\tau \sum_{\sigma=\uparrow,\downarrow} \sum_{\mathbf{k}} \sum_{\zeta=\pm} \varepsilon_{\mathbf{k}}^{(\zeta)} \bar{\psi}_{\mathbf{k},\zeta,\sigma}(\tau) \psi_{\mathbf{k},\zeta,\sigma}(\tau) \\ & + \frac{V}{\sqrt{2N}} \int d\tau \sum_{\sigma=\uparrow,\downarrow} \sum_{\mathbf{k}} [e^{i\mathbf{k}\cdot\mathbf{r}_0} \bar{\psi}_{i,\sigma}(\tau) \psi_{\mathbf{k},\zeta,\sigma}(\tau) \\ & \quad + e^{-i\mathbf{k}\cdot\mathbf{r}_0} \bar{\psi}_{\mathbf{k},\zeta,\sigma}(\tau) \psi_{i,\sigma}(\tau)] \\ & + U \int_0^\beta d\tau \bar{\psi}_{i,\uparrow}(\tau) \bar{\psi}_{i,\downarrow}(\tau) \psi_{i,\downarrow}(\tau) \psi_{i,\uparrow}(\tau). \end{aligned} \quad (\text{A5})$$

Here, $\psi_{i,\sigma}(\tau)$ [$\bar{\psi}_{i,\sigma}(\tau)$] and $\psi_{\mathbf{k},\zeta,\sigma}(\tau)$ [$\bar{\psi}_{\mathbf{k},\zeta,\sigma}(\tau)$] are the Grassman's numbers corresponding to $c_{i,\sigma}$ ($c_{i,\sigma}^\dagger$) and $c_{\mathbf{k},\zeta,\sigma}$ ($c_{\mathbf{k},\zeta,\sigma}^\dagger$), respectively, at imaginary time τ , and β is the inverse temperature. Carrying out the Gaussian integrals over the Grassman's numbers for the conduction electrons, we obtain

$$Z_{\text{AIM}} = C \int \mathcal{D}\bar{\psi}_i \mathcal{D}\psi_i \exp[-S_{\text{imp}}], \quad (\text{A6})$$

where the effective action S_{imp} of the impurity site is given as

$$\begin{aligned} S_{\text{imp}} = & \frac{1}{\beta} \sum_{n=-\infty}^{\infty} \sum_{\sigma=\uparrow,\downarrow} \bar{\psi}_{n,i,\sigma} [-i\omega_n - \varepsilon + \Delta(i\omega_n)] \psi_{n,i,\sigma} \\ & + U \int_0^\beta d\tau \bar{\psi}_{i,\uparrow}(\tau) \bar{\psi}_{i,\downarrow}(\tau) \psi_{i,\downarrow}(\tau) \psi_{i,\uparrow}(\tau) \end{aligned} \quad (\text{A7})$$

with $\omega_n = (2n+1)\pi/\beta$ (n : integer) and C being a constant. Here, we have introduced that

$$\psi_{n,i,\sigma} = \int_0^\beta d\tau e^{i\omega_n \tau} \psi_{i,\sigma}(\tau), \quad (\text{A8})$$

$$\bar{\psi}_{n,i,\sigma} = \int_0^\beta d\tau e^{-i\omega_n \tau} \bar{\psi}_{i,\sigma}(\tau), \quad (\text{A9})$$

and

$$\begin{aligned} \Delta(i\omega_n) = & \frac{V^2}{2N} \sum_{\mathbf{k}} \sum_{\zeta=\pm} \frac{1}{i\omega_n - \varepsilon_{\mathbf{k}}^{(\zeta)}} \\ = & V^2 \int_{-\infty}^{\infty} d\omega \frac{\rho(\omega)}{i\omega_n - \omega}, \end{aligned} \quad (\text{A10})$$

where $\rho(\omega)$ is the local density of states per spin for the conduction band.

Similarly, the partition function for \mathcal{H}_ω in Eq. (5) is given as

$$Z_\omega = \int \mathcal{D}\bar{\psi} \mathcal{D}\psi \exp[-S_\omega], \quad (\text{A11})$$

where

$$\begin{aligned} S_\omega = & \int_0^\beta d\tau \sum_{\sigma=\uparrow,\downarrow} [\bar{\psi}_{i,\sigma}(\tau) (\partial_\tau - \varepsilon) \psi_{i,\sigma}(\tau) \\ & \quad + \int d\omega \bar{\psi}_{\omega,\sigma}(\tau) \partial_\tau \psi_{\omega,\sigma}(\tau)] \\ & + \int_0^\beta d\tau \sum_{\sigma=\uparrow,\downarrow} \int d\omega \omega \bar{\psi}_{\omega,\sigma}(\tau) \psi_{\omega,\sigma}(\tau) \\ & + V \int d\tau \sum_{\sigma=\uparrow,\downarrow} \int d\omega \sqrt{\rho(\omega)} [\bar{\psi}_{i,\sigma}(\tau) \psi_{\omega,\sigma}(\tau) \\ & \quad + \bar{\psi}_{\omega,\sigma}(\tau) \psi_{i,\sigma}(\tau)] \\ & + U \int_0^\beta d\tau \bar{\psi}_{i,\uparrow}(\tau) \bar{\psi}_{i,\downarrow}(\tau) \psi_{i,\downarrow}(\tau) \psi_{i,\uparrow}(\tau) \end{aligned} \quad (\text{A12})$$

and $\psi_{\omega,\sigma}(\tau)$ [$\bar{\psi}_{\omega,\sigma}(\tau)$] is the Grassmann's number corresponding to $a_{\omega,\sigma}$ ($a_{\omega,\sigma}^\dagger$) at imaginary time τ . Carrying

out the Gaussian integral for the conduction band, we can readily show that the effective action S_{imp} of the impurity site is exactly the same as the one for \mathcal{H}_{AIM} with the same $\Delta(i\omega_n)$ given in Eq. (A10). Therefore, as long as the impurity properties are considered, these two models described by Hamiltonians \mathcal{H}_{AIM} and \mathcal{H}_ω are equivalent.

We can follow the same analysis to obtain the effective action of the impurity site for \mathcal{H}_r given in Eq. (7), and find that the effective action is exactly the same as the one in Eq. (A7) except that $\Delta(i\omega_n)$ is now replaced by

$$\Delta_r(i\omega_n) = \sum_{m=1}^M \frac{(\gamma_m^+)^2}{i\omega_n - \xi_m^+} + \sum_{m=1}^M \frac{(\gamma_m^-)^2}{i\omega_n - \xi_m^-} \quad (\text{A13})$$

$$\begin{aligned} &= \sum_{m=1}^M \frac{V^2}{i\omega_n - \xi_m^+} \int_{\omega_m}^{\omega_{m-1}} d\omega \rho(\omega) \\ &+ \sum_{m=1}^M \frac{V^2}{i\omega_n - \xi_m^-} \int_{-\omega_{m-1}}^{-\omega_m} d\omega \rho(\omega). \end{aligned} \quad (\text{A14})$$

Comparing Eqs. (A10) and (A14), we can find that

$$\lim_{M \rightarrow \infty} \Delta_r(i\omega_n) = \Delta(i\omega_n), \quad (\text{A15})$$

provided that $\Lambda \rightarrow 1^+$ is also taken for the logarithmic discretization scheme. Therefore, the effective action S_{imp} of the impurity site for \mathcal{H}_r becomes exactly the same as the one for \mathcal{H}_{AIM} when the small enough energy interval is adopted with $M \rightarrow \infty$ and also $\Lambda \rightarrow 1^+$ for the logarithmic discretization scheme.

Appendix B: Further technical details

In this appendix, we examine further technical details. First, we discuss the l dependence of hopping t_l in \mathcal{H} [Eq. (20)] for the single-impurity Anderson model on the honeycomb lattice. Next, we analyze the convergence behavior of static quantities with respect to L and Λ . We also determine the phase boundary in the thermodynamic limit by explicitly taking the limits of $L \rightarrow \infty$ and $\Lambda \rightarrow 1^+$, which turns out to coincide within our numerical accuracy with the phase boundary obtained by the calculations for $L = 128$ and $\Lambda = 1.15$ in Fig. 3. Finally, we discuss the convergence issue of dynamical quantities.

1. The l dependence of hopping t_l in \mathcal{H}

Let us first show in Fig. 15 the l dependence of t_l , i.e., the nearest-neighbor hopping between the conduction sites in energy space described by \mathcal{H} , for the single-impurity Anderson model on the honeycomb lattice when the logarithmic discretization scheme is used. It is observed in Fig. 15 that t_l decays exponentially with increasing l . Indeed, we find that t_l decays approximately as $t_l \approx \Lambda^{-l/2}$ except for the oscillatory behavior towards one of the edges of the chain opposite to the impurity

site [see also Fig. 1(b)]. Although this oscillatory behavior of t_l is not a major problem for our calculations, we terminate l at $L = M$ to save the computational time. As discussed below, this is rationalized because the physical quantities are already well converged with $L = M$ as long as M is large enough.

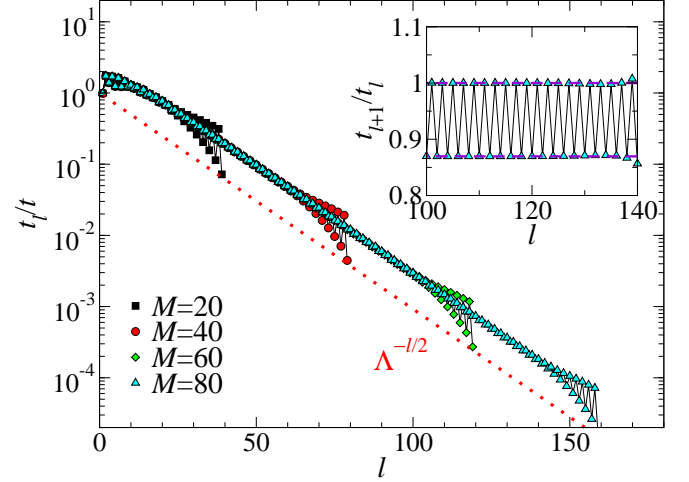


FIG. 15. (Color online) l dependence of t_l in \mathcal{H} for the single-impurity Anderson model on the honeycomb lattice with various values of M indicated in the figure. Note that the maximum value of l for a given M is $2M + 1$. The logarithmic discretization scheme with $\Lambda = 1.15$ is used. A red dotted line indicates $\Lambda^{-l/2}$ with $\Lambda = 1.15$. The inset shows t_{l+1}/t_l for $M = 80$. Two horizontal dashed lines in the inset are $t_{l+1}/t_l = 1$ and Λ^{-1} .

The overall behavior of t_l found in Fig. 15 is in good agreement with the one for the pseudogap Anderson model. It is known that the asymptotic behavior of t_l for the pseudogap Anderson model is

$$t_l \sim \begin{cases} C(\Lambda)\Lambda^{-l/2} & (l : \text{even}), \\ C(\Lambda)\Lambda^{-(l+1)/2} & (l : \text{odd}), \end{cases}, \quad (\text{B1})$$

where $C(\Lambda)$ is a constant depending only on Λ [8]. Therefore, $t_{l+1}/t_l \sim \Lambda^{-1}$ for l even and $t_{l+1}/t_l \sim 1$ for l odd. As shown in the inset of Fig. 15, we find that t_l for the single-impurity Anderson model on the honeycomb lattice also shows the same asymptotic behavior.

In contrast, the l dependence of t_l is qualitatively different when the constant discretization scheme is used. As shown in Fig. 16, t_l is significantly different when different M is used. This is simply because ω_m^\pm for a given m depends directly on M for the constant discretization scheme, while it is independent of M for the logarithmic discretization scheme. We also find in Fig. 16 that the overall behavior of t_l is well described as $t_l \approx W\sqrt{1 - (l/M)^2}/4$. This is a universal feature when the constant discretization scheme is used since the same overall behavior is found even when the constant density of states is assumed.

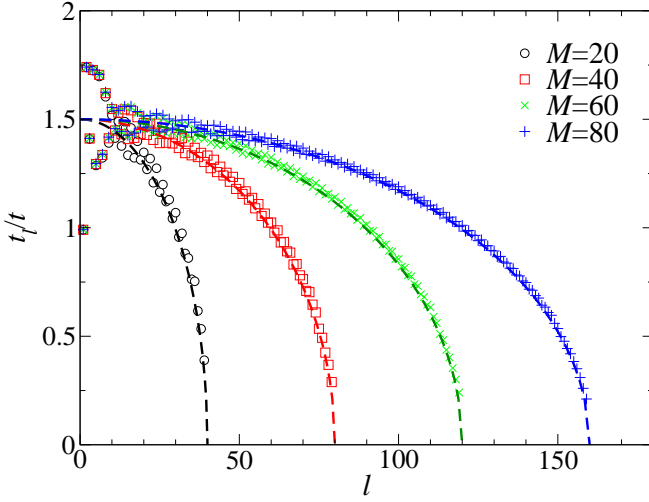


FIG. 16. (Color online) Same as in Fig. 15 but the constant discretization scheme is used. Dashed lines along the symbols indicate $W\sqrt{1-(l/M)^2}/4$.

2. The convergence behavior of static quantities with respect to L and Λ

Next, we examine the L and Λ dependence of the total spin \bar{S}_i at impurity site defined in Eq. (25). In order to show more explicitly the L and Λ dependence, here we shall denote \bar{S}_i as $\bar{S}_i(L, \Lambda)$ when it is calculated using the logarithmic discretization scheme. We find in Fig. 17 that $\bar{S}_i(L, \Lambda)$ for a given Λ is well converged when L is sufficiently large. Note here that we set $M = L$ in Fig. 17. However, the extrapolated value of $\bar{S}_i(L, \Lambda)$ to $L \rightarrow \infty$, i.e.,

$$\bar{S}_i(\Lambda) = \lim_{L \rightarrow \infty} \bar{S}_i(L, \Lambda), \quad (\text{B2})$$

implying that $M \rightarrow \infty$ is also taken with a finite and fixed ratio of M/L , exhibits slight but visible Λ dependence. As shown in the inset of Fig. 17, we find that $\bar{S}_i(\Lambda)$ is almost linearly dependent on Λ when Λ is close to 1, and the difference between $\bar{S}_i(\Lambda)$ with $\Lambda = 1.15$ and the extrapolated value to $\Lambda \rightarrow 1^+$, i.e.,

$$\bar{S}_i^* = \lim_{\Lambda \rightarrow 1^+} \bar{S}_i(\Lambda) \quad (\text{B3})$$

is quite small ($\sim 10^{-3}$). We thus conclude that $\bar{S}_i(\Lambda)$ with $\Lambda = 1.15$ can represent the value in the thermodynamic limit and the corresponding error is as small as 10^{-3} . We should note here that the practical NRG calculations are typically performed with $\Lambda \geq 1.5$ [51].

Next, let us compare the results for the logarithmic discretization scheme and the constant discretization scheme. We indeed find in Fig. 18 that, irrespectively of the discretization schemes, all results converge into a unique value in the limit of $L \rightarrow \infty$ within the error of 10^{-3} . More precisely, the results in Fig. 18 for the logarithmic and constant discretization schemes should

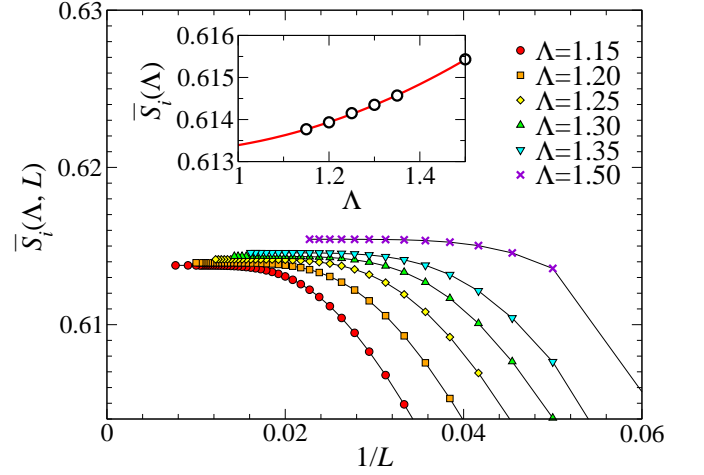


FIG. 17. (Color online) L dependence of the total spin $\bar{S}_i(L, \Lambda)$ at impurity site for the single-impurity Anderson model on the honeycomb lattice at half-filling with $V = t$, $U = 2t$, and $\varepsilon = t$ (i.e., a particle-hole symmetric case). The logarithmic discretization scheme with various Λ (indicated in the figure) is used. Here, we set $M = L$. The inset shows the extrapolated values of $\bar{S}_i(L, \Lambda)$ to $L \rightarrow \infty$, i.e., $\bar{S}_i(\Lambda)$, for six different Λ 's. A red line is a quadratic fit of data.

converge to $\bar{S}_i(\Lambda)$ with $\Lambda = 1.15$ and \bar{S}_i^* , respectively. We also find in Fig. 18 that the ratio M/L , which we set to be 1 in our calculations shown in the main text, does not affect the converged value as long as L and M are sufficiently large. For the logarithmic discretization scheme, the difference for various M/L is found to be as small as 10^{-9} .

3. Phase boundary in the thermodynamic limit

Here, we examine the phase boundary in the thermodynamic limit by explicitly taking the limits of $L \rightarrow \infty$ and $\Lambda \rightarrow 1^+$ for the static quantities, i.e., the local density per spin $\bar{n}_{i\sigma}$ and the total spin \bar{S}_i at the impurity site, calculated using the logarithmic discretization scheme. In order to show explicitly the L and Λ dependence of these quantities, here we adopt the convention used in Eqs. (B2) and (B3). Similarly, we take the limit of $L \rightarrow \infty$ for the local density per spin $\bar{n}_{i\sigma}(L, \Lambda)$ calculated for given L and Λ , i.e.,

$$\bar{n}_{i\sigma}(\Lambda) = \lim_{L \rightarrow \infty} \bar{n}_{i\sigma}(L, \Lambda), \quad (\text{B4})$$

and then take the limit of $\Lambda \rightarrow 1^+$, i.e.,

$$\bar{n}_{i\sigma}^* = \lim_{\Lambda \rightarrow 1^+} \bar{n}_{i\sigma}(\Lambda) \quad (\text{B5})$$

to estimate the value in the thermodynamic limit. To obtain the well-converged and predictive values of $\bar{S}_i(\Lambda)$ and $\bar{n}_{i\sigma}(\Lambda)$ within the residual error of 10^{-5} , L is required as large as 180 for $\Lambda = 1.15$.

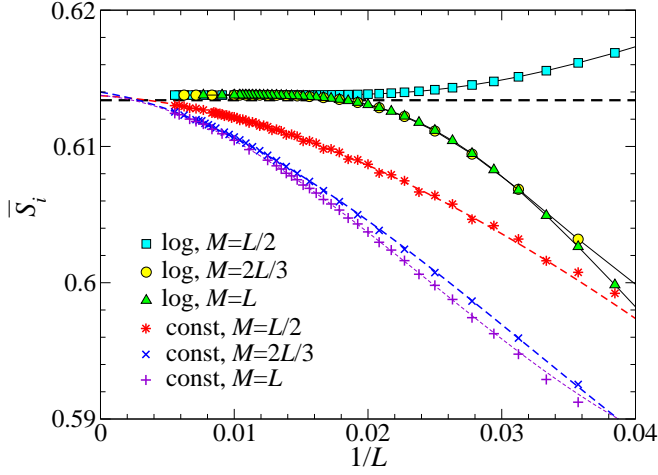


FIG. 18. (Color online) L dependence of the total spin \bar{S}_i at impurity site for the single-impurity Anderson model on the honeycomb lattice at half-filling with $V = t$, $U = 2t$, and $\varepsilon = t$ (i.e., a particle-hole symmetric case). Here, we use both logarithmic and constant discretization schemes, denoted as “const” and “log,” respectively, with $M = L/2$, $2L/3$, and L . We set $\Lambda = 1.15$ for the logarithmic discretization scheme. Dashed lines along the symbols for the constant discretization scheme are fitting curvatures with cubic polynomials of $1/L$. A black dashed line indicates the extrapolated value \bar{S}_i^* to $L \rightarrow \infty$ and $\Lambda \rightarrow 1^+$ obtained in the inset of Fig. 17.

Typical results around the phase boundary are shown in Figs. 19 and 20. We find in Figs. 19 and 20 that $\bar{n}_{i\sigma}(\Lambda)$ and $\bar{S}_i(\Lambda)$ exhibit the abrupt changes exactly at the same ε , i.e., $\varepsilon_c(\Lambda)$, for each Λ , although $\varepsilon_c(\Lambda)$ itself depends clearly on Λ . The phase boundary in the thermodynamic limit is thus obtained by extrapolating $\varepsilon_c(\Lambda)$ to $\Lambda \rightarrow 1^+$, i.e.,

$$\varepsilon_c^* = \lim_{\Lambda \rightarrow 1^+} \varepsilon_c(\Lambda). \quad (\text{B6})$$

As shown in the inset of Fig. 20, we find that $\varepsilon_c^* = 1.707t \pm 0.001t$ for $V = t$ and $U = 2t$, which is in excellent agreement with $\varepsilon_c = 1.707t - 1.708t$ estimated from the results for $L = 128$ and $\Lambda = 1.15$ in the main text (Figs. 3 and 5). We should also note that ε_c is very close to $\varepsilon_c(\Lambda) = 1.708 - 1.709t$ for $\Lambda = 1.15$. Therefore, we conclude that the typical error of the phase boundary ε_c obtained in Figs. 3 and 5 is as small as $0.002t$.

4. Convergence behavior of dynamical quantities

Finally, we discuss the convergence of the dynamical quantities $\chi_s(\omega)$ and $\chi_c(\omega)$ for a given broadening factor η . In order to make an accurate comparison, here we consider the noninteracting limit. In this limit, the spin excitation spectrum at the impurity site is given as

$$\chi_0(\omega) = \frac{\eta}{2\pi} \sum_{e_k < \mu} \sum_{e_{k'} > \mu} \frac{|u_i^{(k)} u_i^{(k')}|^2}{(\omega - e_k + e_{k'})^2 + \eta^2}, \quad (\text{B7})$$

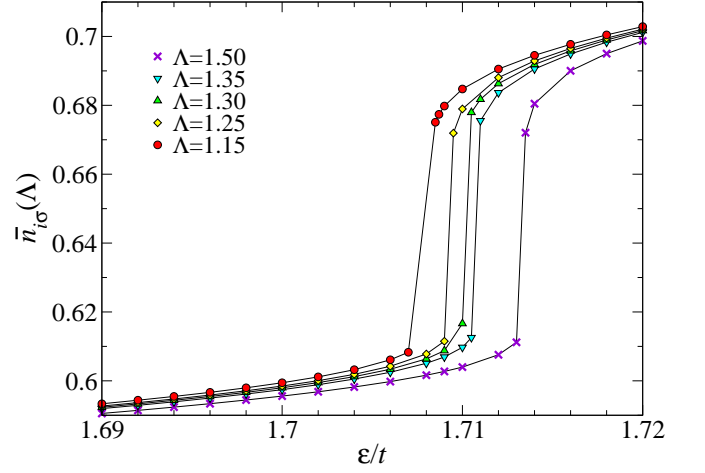


FIG. 19. (Color online) Local density per spin $\bar{n}_{i\sigma}(\Lambda)$ at impurity site for the single-impurity Anderson model on the honeycomb lattice at half-filling with $V = t$ and $U = 2t$. The logarithmic discretization scheme with various Λ (indicated in the figure) is used.

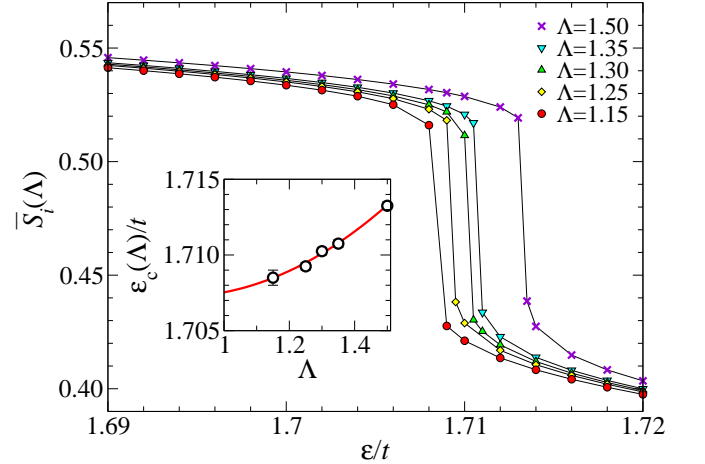


FIG. 20. (Color online) Total spin $\bar{S}_i(\Lambda)$ at impurity site for the single-impurity Anderson model on the honeycomb lattice at half-filling with $V = t$ and $U = 2t$. The logarithmic discretization scheme with various Λ (indicated in the figure) is used. The inset shows $\varepsilon_c(\Lambda)$ at which the abrupt change of $\bar{n}_{i\sigma}(\Lambda)$ and $\bar{S}_i(\Lambda)$ occurs with varying ε . A red line is a fitting curve with a quadratic polynomial of Λ .

where $u_i^{(k)}$ is the impurity site component of the k th eigenstate of \hat{H}'_0 in Eq. (18) with its eigenvalue e_k . The charge excitation spectrum at the impurity site is expressed with the same form as in Eq. (B7) except for the additional factor 4, i.e., $\chi_c(\omega) = 4\chi_0(\omega)$, in the noninteracting limit. Therefore, we only consider $\chi_0(\omega)$ below.

As shown in Fig. 21, we find that $\chi_0(\omega)$ for smaller L exhibits oscillating behavior when the constant discretization scheme is used. This is simply understood because the broadening factor η is smaller than the level

spacing of e_k when L is small. Therefore, the absence of such oscillating behavior for large enough L is a hall-mark of the convergence for a given η . Indeed, we find in Fig. 21 that $\chi_0(\omega)$ for $L = 100$ is well converged, as compared with that for $L = 1000$, and the estimated error is as small as 10^{-3} .

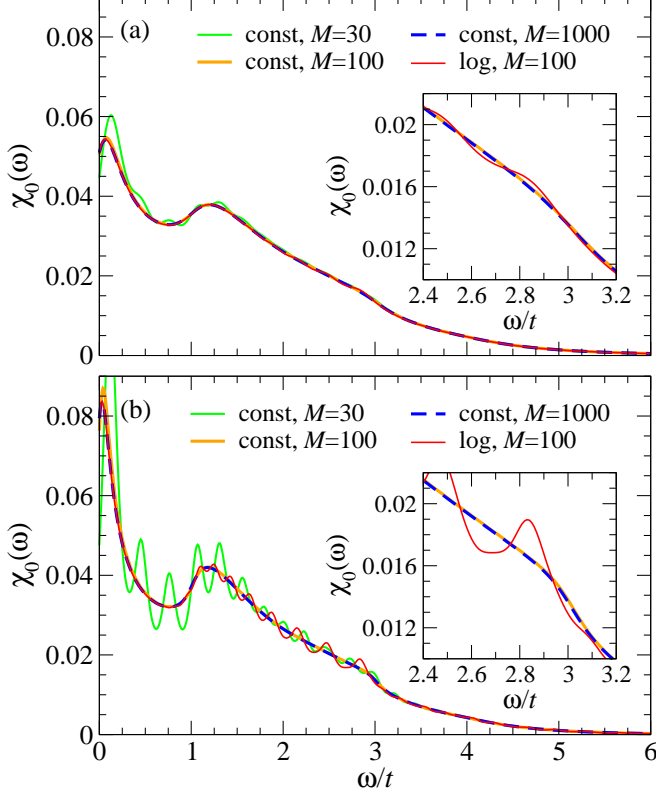


FIG. 21. (Color online) Spin and charge excitation spectrum $\chi_0(\omega)$ at the impurity site in the noninteracting limit for the single-impurity Anderson model on the honeycomb lattice at half-filling with $V = t$ and $\varepsilon = 0$. Here, we use both constant and logarithmic discretization schemes, denoted as “const” and “log,” respectively, with $M = L$ and broadening factors $\eta = 0.2t$ (a) and $0.1t$ (b). We set $\Lambda = 1.15$ for the logarithmic discretization scheme. The insets show the enlarged scale around $\omega \sim 2.4\text{--}3.2t$. For clarity, the results for the constant discretization scheme with $M = 20$ and 40 are not shown.

We also notice in the insets of Fig. 21 that the similar oscillating behavior appears in the high-energy regions when the logarithmic discretization scheme is employed. This oscillating behavior is absent in the constant discretization scheme when the same M is used. This is simply because, in the logarithmic discretization scheme, the energy mesh size is determined by Λ and becomes wider in the higher-energy regions than in the lower-energy regions. In contrast, in the constant discretization scheme, the energy mesh size is constant for all energy regions and becomes smaller with increasing M .

Aside from the slow convergence problem in the high energy regions, there is a more serious technical issue for the logarithmic discretization scheme. In the dynamical

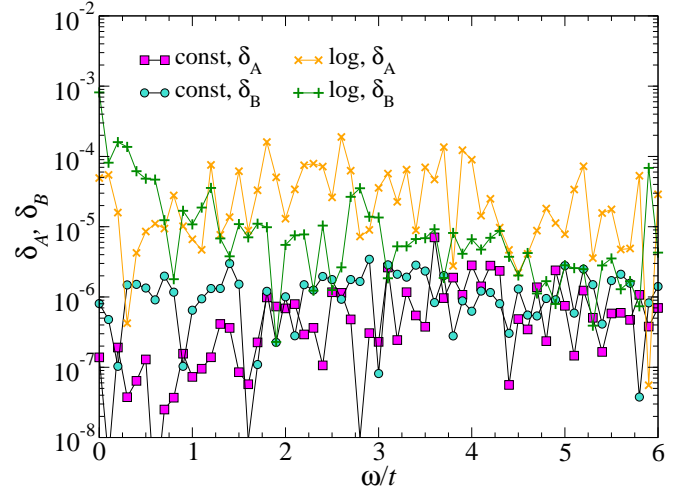


FIG. 22. (Color online) δ_A and δ_B , defined in Eqs. (B12) and (B13), respectively, in the non-interacting limit for the single-impurity Anderson model on the honeycomb lattice at half-filling with $V = t$ and $\varepsilon = 0$. Here, we use both constant and logarithmic discretization schemes, denoted as “const” and “log,” respectively, with $M = L = 100$ and a broadening factor $\eta = 0.2t$. We set $\Lambda = 1.15$ for the logarithmic discretization scheme. These results are obtained by performing six sweeps of the DMRG iteration with keeping $m_D = 1400$.

DMRG calculation for, e.g., the spin excitation spectrum $\chi_s(\omega)$ at the impurity site, we have to construct the reduced density matrix of a mixed state composed of the ground state $|\psi_0\rangle$ and the two excited states,

$$|A\rangle = S_i^z |\psi_0\rangle \quad (\text{B8})$$

and

$$|B\rangle = \frac{1}{(\omega - \mathcal{H} + E_0)^2 + \eta^2} S_i^z |\psi_0\rangle, \quad (\text{B9})$$

for each ω . Therefore, as compared with the ground state calculation, the convergence of the dynamical calculation is slower with respect to the number m_D of the reduced density matrix eigenstates kept in the DMRG calculation. This is an additional source of numerical errors and depends sensitively on the discretization schemes.

Since

$$\langle A|A\rangle = \langle \psi_0 | S_i^z S_i^z | \psi_0 \rangle = \frac{\bar{S}_i}{3} \quad (\text{B10})$$

and

$$\frac{\eta}{\pi} \langle B | [(\omega - \mathcal{H} + E_0)^2 + \eta^2] | B \rangle = \chi_s(\omega), \quad (\text{B11})$$

we can infer for each ω the errors in the two excited states $|A\rangle$ and $|B\rangle$ by evaluating

$$\delta_A = \left| \langle A|A\rangle - \frac{\bar{S}_i}{3} \right| \quad (\text{B12})$$

and

$$\delta_B = \left| \frac{\eta}{\pi} \langle B | [(\omega - \mathcal{H} + E_0)^2 + \eta^2] | B \rangle - \chi_s(\omega) \right| \quad (\text{B13})$$

in the non-interacting limit, where $\chi_s(\omega)$ is known exactly in Eq. (B7) and $\bar{S}_i = 1.5$ when the particle-hole symmetry is preserved.

Figure 22 shows the results of δ_A and δ_B for the constant and logarithmic discretization schemes with keeping the same number m_D of the reduced density matrix eigenstates and the same tolerance for the optimization of $|\psi_0\rangle$ and $|B\rangle$ [34]. As shown in Fig. 22, we find that both δ_A and δ_B for the logarithmic discretization

scheme are larger than those for the constant discretization scheme. These results clearly show that the convergence of the excited states in the logarithmic discretization scheme is slow and thus a larger m_D is required to reach the same convergence as in the constant discretization scheme, implying that the logarithmic discretization scheme demands more computational cost. Therefore, we employ the constant discretization scheme to calculate the full excitation spectra.

-
- [1] K. M. McCreary, A. G. Swartz, W. Han, J. Fabian, and R. K. Kawakami, *Phys. Rev. Lett.* **109**, 186604 (2012).
 - [2] R. R. Nair, M. Sepioni, I.-L. Tsai, O. Lehtinen, J. Keinonen, A. V. Krashennnikov, T. Thomson, A. K. Geim, and I. V. Grigorieva, *Nat. Phys.* **8**, 199 (2012).
 - [3] A. H. C. Neto, F. Guinea, N. M. R. Peres, K. S. Novoselov, and A. K. Geim, *Rev. Mod. Phys.* **81**, 109 (2009).
 - [4] L. Fritz and M. Vojta, *Rep. Prog. Phys.* **76**, 032501 (2013).
 - [5] M. Vojta and L. Fritz, *Phys. Rev. B* **70**, 094502 (2004).
 - [6] L. Fritz and M. Vojta, *Phys. Rev. B* **70**, 214427 (2004).
 - [7] C. Gonzalez-Buxton and K. Ingersent, *Phys. Rev. B* **57**, 14254 (1998).
 - [8] R. Bulla, T. Pruschke, and C. Hewson, *J. Phys.: Cond. Mat.* **9**, 10463 (1997).
 - [9] R. Bulla, M. T. Glossop, D. E. Logan, and T. Pruschke, *J. Phys.: Cond. Mat.* **12**, 4899 (2000).
 - [10] K. Ingersent and Q. Si, *Phys. Rev. Lett.* **89**, 076403 (2002).
 - [11] T. Kanao, H. Matsuura, and M. Ogata, *J. Phys. Soc. Jpn.* **81**, 063709 (2012).
 - [12] H. Li and F. D. M. Haldane, *Phys. Rev. Lett.* **101**, 010504 (2008).
 - [13] L. Fidkowski, *Phys. Rev. Lett.* **104**, 130502 (2010).
 - [14] F. Pollmann, A. M. Turner, E. Berg, and M. Oshikawa, *Phys. Rev. B* **81**, 064439 (2010).
 - [15] T. Yoshida, R. Peters, S. Fujimoto, and N. Kawakami, *Phys. Rev. Lett.* **112**, 196404 (2014).
 - [16] S. Ejima, F. Lange, and H. Fehske, *Phys. Rev. Lett.* **113**, 020401 (2014).
 - [17] I. Affleck, *Acta Phys. Pol. B* **26**, 1869 (1995).
 - [18] A. Bayat, H. Johannesson, S. Bose, and P. Sodano, *Nat. Comm.* **5**, 3784 (2014).
 - [19] M. Vojta, *Phil. Mag.* **86**, 1807 (2006).
 - [20] S. R. White, *Phys. Rev. Lett.* **69**, 2863 (1992).
 - [21] S. R. White, *Phys. Rev. B* **48**, 10345 (1993).
 - [22] A. Chandran, V. Khemani, and S.L. Sondhi, *Phys. Rev. Lett.* **113**, 060501 (2014).
 - [23] K. G. Wilson, *Rev. Mod. Phys.* **47**, 773 (1975).
 - [24] R. Bulla, T. A. Costi, and T. Pruschke, *Rev. Mod. Phys.* **80**, 395 (2008).
 - [25] G. Lehmann, P. Rennert, M. Taut, and H. Wonn, *Phys. Status Solidi* **37**, K27 (1970); G. Lehmann and M. Taut, *ibid.* **54**, 469 (1972).
 - [26] O. Jepsen and O. K. Andersen, *Solid State Comm.* **9**, 1763 (1971).
 - [27] J. K. Cullum and R. A. Willoughby, *Lanczos Algorithms for Large Symmetric Eigenvalue Computations* (Birkhäuser, Boston, 1985).
 - [28] D. J. García, K. Hallberg, and M. J. Rozenberg, *Phys. Rev. Lett.* **93**, 246403 (2004).
 - [29] R. Peters, *Phys. Rev. B* **84**, 075139 (2011).
 - [30] T. Shirakawa and S. Yunoki, *Phys. Rev. B* **90**, 195109 (2014).
 - [31] C. A. Büsser, G. B. Martins, and A. E. Feiguin, *Phys. Rev. B* **88**, 245113 (2013).
 - [32] A. Allerdt, C. A. Büsser, G. B. Martins, and A. E. Feiguin, *Phys. Rev. B* **91**, 085101 (2015).
 - [33] See, e.g., A. C. Hewson, *The Kondo Problem to Heavy Fermions* (Cambridge University Press, New York, 1997).
 - [34] E. Jeckelmann, *Phys. Rev. B* **66**, 045114 (2002).
 - [35] To be more precise, these three lowest entanglement levels are still quasi degenerate at $\varepsilon = 1.707t$ as $\xi_1 = \xi_2 = 1.429$ and $\xi_3 = 1.609$. When we increase ε slightly to $1.708t$, we find that $\xi_1 = 1.292$ and $\xi_2 = \xi_3 = 1.584$. Further fine tuning of ε is required to reach at the exact three fold degenerate point, corresponding to the VF point at the phase boundary.
 - [36] When l_L is even and L is finite, $|\bar{\psi}_1\rangle \sim |\phi_\uparrow\rangle_L \otimes |0\rangle_R$ and $|\bar{\psi}_2\rangle \sim |\phi_\downarrow\rangle_L \otimes |0\rangle_R$ are entangled, where $|\phi_{\uparrow(\downarrow)}\rangle_L \sim |\uparrow(\downarrow)\rangle_i \otimes |\downarrow(\uparrow)\rangle_{\bar{L}}$ and $|s\rangle_{\bar{L}}$ with $s = \uparrow, \downarrow, 0$ represents the z component of total spin ($Sz = 1/2, -1/2, 0$) in the left block excluding the impurity site. Therefore, the ground state is represented approximately as $|\psi_0\rangle \sim \frac{1}{\sqrt{2}}(|\psi_1\rangle - |\psi_2\rangle) \sim \frac{1}{\sqrt{2}}(|\phi_\uparrow\rangle_L - |\phi_\downarrow\rangle_L) \otimes |0\rangle_R$. We can now easily show that the lowest ξ_k for $|\psi_0\rangle$ is singlet.
 - [37] In the ASC phase for $\varepsilon > U/2$, we find that the lowest entanglement level is non degenerate for both even and odd l_L . This is because the total number of electrons in the left block is l_L for l_L even and $l_L + 1$ for l_L odd.
 - [38] Z. Y. Meng, T. C. Lang, S. Wessel, F. F. Assaad, and A. Muramatsu, *Nature* **464**, 847851 (2010).
 - [39] S. Sorella, Y. Otsuka, and S. Yunoki, *Sci. Rep.* **2**, 992 (2012).
 - [40] F. F. Assaad and I. F. Herbut, *Phys. Rev. X* **3**, 031010 (2013).
 - [41] F. Parisen Toldin, M. Hohenadler, F. F. Assaad, and I. F. Herbut, *Phys. Rev. B* **91**, 165108 (2015).
 - [42] Y. Otsuka, S. Yunoki, and S. Sorella, *Phys. Rev. X* **6**, 011029 (2016).
 - [43] W. Han, R. K. Kawakami, M. Gmitra, and J. Fabian, *Nat. Nanotechnology* **9**, 794 (2014).
 - [44] A. H. Castro Neto and F. Guinea, *Phys. Rev. Lett.* **103**, 026804 (2009).
 - [45] M. J. Schmidt and D. Loss, *Phys. Rev. B* **81**, 165439 (2010).
 - [46] C. Weeks, J. Hu, J. Alicea, M. Franz, and R. Wu, *Phys. Rev. X* **1**, 021001 (2011).

- [47] J. Zhou, Q. F. Liang, and J. M. Dong, *Carbon* **48**, 1405 (2010).
- [48] J. Balakrishnan, G. K. W. Koon, M. Jaiswal, A. H. Castro Neto, and B. Özyilmaz, *Nat. Physics* **9**, 284 (2013).
- [49] D. Marchenko, A. Varykhalov, M. R. Scholz, G. Bihlmayer, E. I. Rashba, A. Rybkin, A. M. Shikin, and O. Rader, *Nat. Comm.* **3**, 1232 (2012).
- [50] D. Mastrogiuseppe, A. Wong, K. Ingersent, S. E. Ulloa, and N. Sandler, *Phys. Rev. B* **90**, 035426 (2014).
- [51] Ž. Osolin and R. Žitko, *Phys. Rev. B* **87**, 245135 (2013).